Performance, Stability, and Plume Characterization of the HERMeS Thruster with Boron Nitride Silica Composite Discharge Channel

IEPC-2017-392

Presented at the 35th International Electric Propulsion Conference
Georgia Institute of Technology • Atlanta, Georgia • USA
October 8 – 12, 2017

Hani Kamhawi[1], Wensheng Huang[2], James Gilland[3], Thomas Haag[4], Jonathan Mackey[5], John Yim[6], Luis Pinero[7], George Williams[8], Peter Peterson[9], and Daniel Herman[10]
NASA Glenn Research Center, Cleveland, OH, 44135, USA

Abstract: NASA's Hall Effect Rocket with Magnetic Shielding (HERMeS) 12.5kW Technology Demonstration Unit-3 (TDU-3) has been the subject of extensive technology maturation in preparation for flight system development. Detailed performance, stability, and plume characterization tests of the thruster were performed at NASA GRC's Vacuum Facility 5 (VF-5). The TDU-3 thruster implements a magnetic topology that is identical to TDU-1. The TDU-3 boron nitride silica composite discharge channel material is different than the TDU-1 heritage boron nitride discharge channel material. Performance and stability characterization of the TDU-3 thruster was performed at discharge voltages between 300V and 600V and at discharge currents between 5A and 21.8A. The thruster performance and stability were assessed for varying magnetic field strength, cathode flow fractions between 5% and 9%, varying harness inductance, and for reverse magnet polarity. Performance characterization test results indicate that the TDU-3 thruster performance is in family with the TDU-1 levels. TDU-3's thrust efficiency of 65% and specific impulse of 2,800sec at 600V and 12.5kW exceed performance levels of SOA Hall thrusters. Thruster stability regimes were characterized with respect to the thruster discharge current oscillations (discharge current peak-to-peak and root mean square magnitudes), discharge current waveform power spectral density analysis, and maps of the current-voltage-magnetic field. Stability characterization test results indicate a stability profile similar to TDU-1. Finally, comparison of the TDU-1 and TDU-3 plume profiles found that there were negligible differences in the plasma plume characteristics between the TDU with heritage boron nitride versus the boron nitride silica composite discharge channel.

I.Introduction

For missions beyond low Earth orbit, spacecraft size and mass can be dominated by onboard chemical propulsion systems and propellants that may constitute more than 50% of spacecraft mass. This impact can be substantially

[1] Senior Research Engineer, Electric Propulsion Systems Branch, Hani,Kamhawi-1@nasa.gov.
[2] Research Engineer, Electric Propulsion Systems Branch, Wensheng.Huang@nasa.gov.
[3] Senior Research Engineer, Ohio Aerospace Institute, James.H.Gilland@nasa.gov.
[4] Senior Research Engineer, Electric Propulsion Systems Branch, Thomas.W.Haag@nasa.gov.
[5] Research Engineer, Electric Propulsion Systems Branch, Jonathan.A.Mackey@nasa.gov.
[6] Senior Research Engineer, Electric Propulsion Systems Branch, John.T.Yim@nasa.gov.
[7] Senior Research Engineer, Electric Propulsion Systems Branch, Luis.R.Pinero@nasa.gov.
[8] Senior Research Engineer, Electric Propulsion Systems Branch, George.J.Williams@nasa.gov.
[9] Senior Research Engineer, Vantage Partners, LLC, Peter.Y.Peterson@nasa.gov.
[10] Program Manager, Electric Propulsion Systems Branch, Daniel.A.Herman@nasa.gov.

reduced through the utilization of Solar Electric Propulsion (SEP) due to its substantially higher specific impulse. Studies performed for NASA's Human Exploration and Operations Mission Directorate (HEOMD) and Science Mission Directorate have demonstrated that a 40kW-class SEP capability can be enabling for both near term and future architectures and science missions.[1]

Since 2012 NASA has been developing a 14kW Hall thruster electric propulsion string that can serve as the building block for realizing a 40 kW-class SEP capability. NASA continues to evolve a human exploration approach for beyond low-Earth orbit and to do so, where practical, in a manner involving international, academic, and industry partners.[2] NASA publicly presented a reference exploration concept at the HEOMD Committee of the NASA Advisory Council meeting on March 28, 2017.[3] This approach is based on an evolutionary human exploration architecture, depicted in Fig. 1, expanding into the solar system with cis-lunar flight testing and validation of exploration capabilities before crewed missions beyond the earth-moon system and eventual crewed Mars missions. One of the key objectives is to achieve human exploration of Mars and beyond through the prioritization of those technologies and capabilities best suited for such a mission in accordance with the stepping stone approach to exploration.[4] High-power solar electric propulsion is one of those key technologies that has been prioritized because of its significant exploration benefits. A high-power, 40 kW-class Hall thruster propulsion system provides significant capability and represents, along with flexible blanket solar array technology, a readily scalable technology with a clear path to much higher power systems.[5]

The 14 kW Hall thruster system development, led by the NASA Glenn Research Center (GRC) and the Jet Propulsion Laboratory (JPL), began with maturation of the high-power Hall thruster and power processing unit. The technology development work has transitioned to Aerojet Rocketdyne via a competitive procurement selection for the Advanced Electric Propulsion System (AEPS) contract. The AEPS contract includes the development, qualification, and multiple flight 14 kW electric propulsion string deliveries.[6] The AEPS Electric Propulsion (EP) string consists of the Hall thruster, power processing unit (including digital control and interface functionality), xenon flow controller, and associated intra-string harnesses. NASA continues to support the AEPS development leveraging in-house expertise, plasma modeling capability, and world-class test facilities. NASA also executes AEPS and mission risk reduction activities to support the AEPS development and mission application.[7]

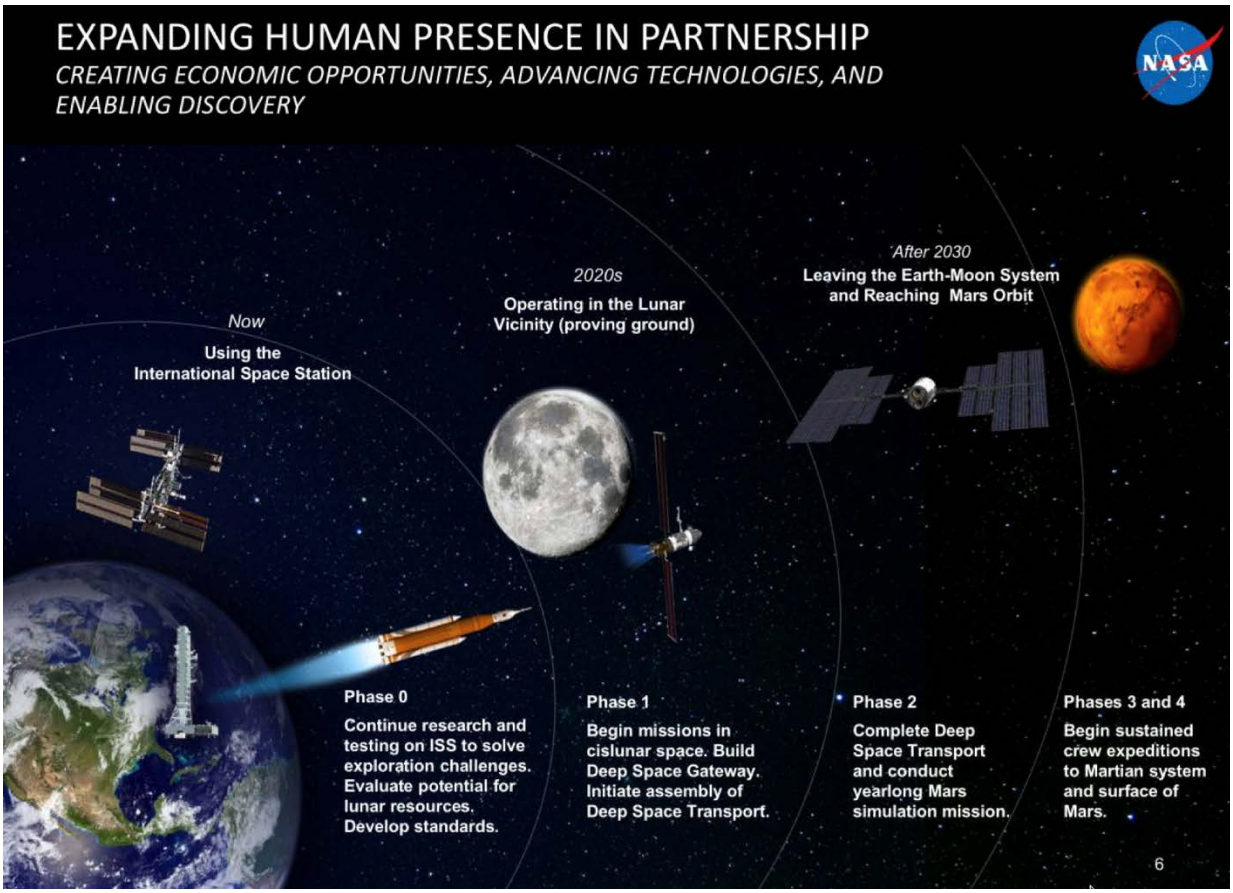

Figure 1. NASA Human Exploration Vision including Deep Space Gateway (DSG) and Deep Space Transport (DST).[2]

II.Background

NASA's Hall Effect Rocket with Magnetic Shielding (HERMeS) 12.5 kW TDU-1 has been the subject of extensive technology maturation in preparation for flight system development starting in 2014.[8,9,10,11,12] A number of tests were performed on the thruster, the results of these tests were presented in 2016.[13,14,15,16,17,18] The TDU-1 thruster employed a heritage boron nitride (BN) discharge channel material. Part of the technology maturation effort included an evaluation of thruster operation with conducting and dielectric front pole cover materials in three different electrical configurations. Part of the test campaign involved performing extensive performance, stability, and pressure characterization of the TDU-1 thruster.

A graphite front pole cover thruster configuration with the thruster body electrically tied to cathode and an alumina front pole cover thruster configuration with the thruster body floating were evaluated.[13,14] Performance characterization tests found that higher thruster performance was attained with the graphite front pole cover configuration and the thruster electrically tied to cathode. A total thrust efficiency of 68% and a total specific impulse of 2,820sec were demonstrated at a discharge voltage of 600V and a discharge power of 12.5kW. Thruster stability regimes were characterized with respect to the thruster discharge current oscillations (discharge current peak-to-peak (Pk2Pk) and root mean square (RMS) magnitudes), along with maps of the current-voltage-magnetic field (IVB). Analysis of TDU-1 discharge current waveforms found that slightly lower discharge current Pk2Pk and RMS magnitudes were attained when the thruster was electrically floated with alumina front pole covers.[13]

In addition, both electrical configurations were evaluated at different facility pressure conditions to determine effects on thruster operation.[13,15] Thruster performance and stability were shown to be mostly invariant to changes in the facility background pressure for pressures below 1×10^{-5} Torr-Xe (for thruster flow rates of 20.2mg/s and above). Power spectral density (PSD) analysis of the discharge current waveforms found that increasing the background pressure resulted in a higher discharge current dominant frequency with the PSD profiles shifting to the right with increased facility background pressure. Finally, the IVB maps of the TDU-1 thruster at elevated background pressures

showed that the discharge current became more oscillatory at lower thruster mass flow rates and that thruster operation at higher flow rates resulted in less change to the thruster's IVB characteristics.[13]

The results reported in this paper are for tests performed on the TDU-3 thruster. The key TDU-3 thruster design features are identical to TDU-1 with the exception of the discharge channel BN material grade. Boron nitride hot-pressed with a binder (designated hereafter as heritage BN) has historically been the material of choice for the discharge chamber, but an alternative BN silica composite material is being considered. Bulk properties of the two ceramics vary with composition, temperature, and orientation so direct comparisons between alternative grades is complicated, but general trends can be used a deciding metrics. Wherever possible, transport properties, bulk properties, and microstructures of the ceramics have been evaluated in house by NASA GRC and JPL. In general, the electrical properties of interest to Hall thrusters of both grades of ceramic are very comparable across a wide range of frequencies. Similarly, the thermal properties including emissivity, diffusivity, conductivity, thermal expansion coefficient, and specific heat are comparable within similar orientations of the two grades. The mechanical properties including flexural strength and elastic modulus are also comparable in similar orientations at room temperature. The high temperature flexural strength of the heritage BN is found to be significantly reduced compared to the BN silica composite. In terms of bulk properties including the density, open pore porosity, and moisture absorption of the two BN grades differ. The BN silica composites have a less porous structure and absorb less moisture during high humidity exposure compared to the heritage ceramic. The moisture sensitivity of the ceramic is of critical interest as bake-out, handling, and storage procedures all must be tailored to the sensitivity of the ceramic. Given the similarity of electrical, thermal, and mechanical properties and the difference in moisture sensitivity the BN silica composites are appearing to be a good alternative to heritage. Additional work studying the fracture toughness and slow crack growth of the ceramics must still be evaluated, along with batch to batch repeatability studies.

The objective of this paper is to present a detailed characterization and evaluation of the TDU-3 thruster with the BN silica composite discharge channel. A companion paper by Williams presents the results of a series of short duration wear tests of the TDU-3.[19]

The following sections in the paper present the experimental apparatus and the test results. The test results are presented in 3 sections. In Section IV, the thruster's performance results are presented for the reference firing conditions (RFCs), thruster magnetic mapping, cathode flow fraction variation tests, harness inductance variation tests, and for the reverse magnet polarity tests. Section V presents the thruster's stability characterization results for the tests presented in Section IV; the results include plots of discharge current Pk2Pk, discharge current RMS, discharge voltage Pk2Pk, discharge voltage RMS, discharge current PSD analysis, and IVB maps at selected flow rates. Section VI presents comparisons of selected TDU-1 and TDU-3 plume profiles. Finally, Section VII presents th e conclusions and summary from this test campaign.

III.Experimental Apparatus

A. Hall Effect Rocket with Magnetic Shielding TDU-3

The design of HERMeS TDU-3 incorporates technologies developed by NASA over nearly two decades. The thruster incorporates a magnetic shielding topology to eliminate discharge channel erosion as a life limiting mechanism.[20,21,22,23] The result is a significant increase in the operational lifetime, with HERMeS being designed to operate at 3,000sec specific impulse and a projected life of > 50,000hrs. The TDU-3 thruster maintained TDU-1 key design features which include: magnetic field topology, propellant manifold design, and discharge channel dimensions. The key difference between the TDU-1 and TDU-3 thruster was the grade of the discharge channel BN material; for TDU-1 it was heritage BN and for TDU-3 a BN silica composite was used. The 12.5 kW HERMeS TDU-3 was installed inside Vacuum Facility (VF-5) at NASA GRC.

Figure 2. TDU-3 installed in NASA GRC VF-5.

A. Vacuum Facility

Testing of the HERMeS TDU-3 thruster was performed in VF-5 at NASA GRC.[24] Figure 2 shows the VF-5 graphite

lined chamber walls. Full details on the facility can be found in Ref. 25. The VF-5 main chamber is 4.6 m in diameter, 18.3 m long, and can be evacuated with cryopanels and/or oil diffusion pumps. For the test campaign discussed in this paper, the TDU-3 Hall thruster was located in the main volume of the chamber to ensure the lowest possible background pressure during thruster operation.[26] Facility pressure was monitored with three xenon and one air calibrated ion gauges (IGs) during thruster operation. Ion gauge 3 (located 1m radially away from thruster's exit plane at 3 o'clock position) was employed as the main pressure reading during operation based on the modeling results and experimental experience indicating that it provides the most representative reading of the facility background pressure.[26]

B. Power Supplies, Data Acquisition, and Control Systems

For the HERMeS TDU-3 test campaign the thruster was powered with a laboratory power rack that contained the discharge, inner and outer electromagnet, cathode heater, and cathode keeper power supplies. The discharge power supply consists of three 15kW (1000V and 15A) power supplies that were connected in a master-slave configuration. A computer was used to sweep the thruster discharge voltage during the thruster IVB maps.

The data acquisition system used for the TDU-3 tests was a multiplexed datalogger with computer interface. The datalogger monitored the voltages, currents, temperatures, propellant flow rates, chamber pressure, and thrust at 1 Hz during performance testing. The computer interface had the additional benefit of allowing a number of channels to be monitored with failsafe limits for unattended operation. The uncertainties of the data logger measurements were ±0.05% for the voltage and current measurements.

C. Flow System

A laboratory propellant feed system was used in the TDU-3 test campaign. The feed system supplied xenon to the thruster and was also used to elevate the facility background pressure. The propellant feed system utilized four mass flow controllers (MFC). A 500 and 100sccm MFCs supplied xenon propellant to the thruster and cathode, respectively. A 200 and 1,000sccm MFCs supplied xenon to elevate the chamber pressure, its auxiliary flow was injected at mid chamber and was directed toward the chamber end cap opposite to thruster location. The MFCs calibration curves indicated that the anode and cathode flow rate uncertainties are ≤1% of the set value.

D. Diagnostics

1. Thrust Stand

The performance of the TDU-3 Hall thruster was measured with an inverted pendulum null-type thrust stand. The NASA GRC high-power thrust stand has an accuracy of ≤1% based on a statistical analysis of the calibration and thrust zero data taken throughout the test campaign. The operation and theory of the inverted pendulum null-type thrust stand are described in detail in Refs. 27 and 28. The high-power thrust stand was operated in a null-type configuration, which allows the thruster to remain stationary while testing. The thrust stand was also equipped with a closed loop inclination control circuit, which utilized a piezoelectric element to minimize thermal drift during thruster tests. The thrust stand was calibrated in-situ with known masses on a pulley system connected to a stepper motor. The thrust stand was calibrated before and after each performance mapping period.

2. Plasma Plume

This section briefly describes the plasma diagnostics deployed during testing. The plasma diagnostics deployed included a Faraday probe (FP), a Langmuir probe (LP), a retarding potential analyzer (RPA), and a Wien filter spectrometer (WFS). All probes were biased with commercially available power supplies.

Figure 3 (left) shows a photograph of the probe package and the relative position of the four probes in the package. Spatial offset between the probes were accounted for when positioning the probes so that data from different probes can be correlated. Both the RPA and WFS were protected by independent shutters. The probe package was mounted on a boom arm, which was mounted on a set of commercially available motion stages that provided polar and radial motion. Positioning accuracy of this motion system was <1 mm for the radial axis and <0.2° for the polar axis. The probe package, boom arm, and the bottom of the motion stages were shielded with Grafoil to reduce the amount of backsputtered material.

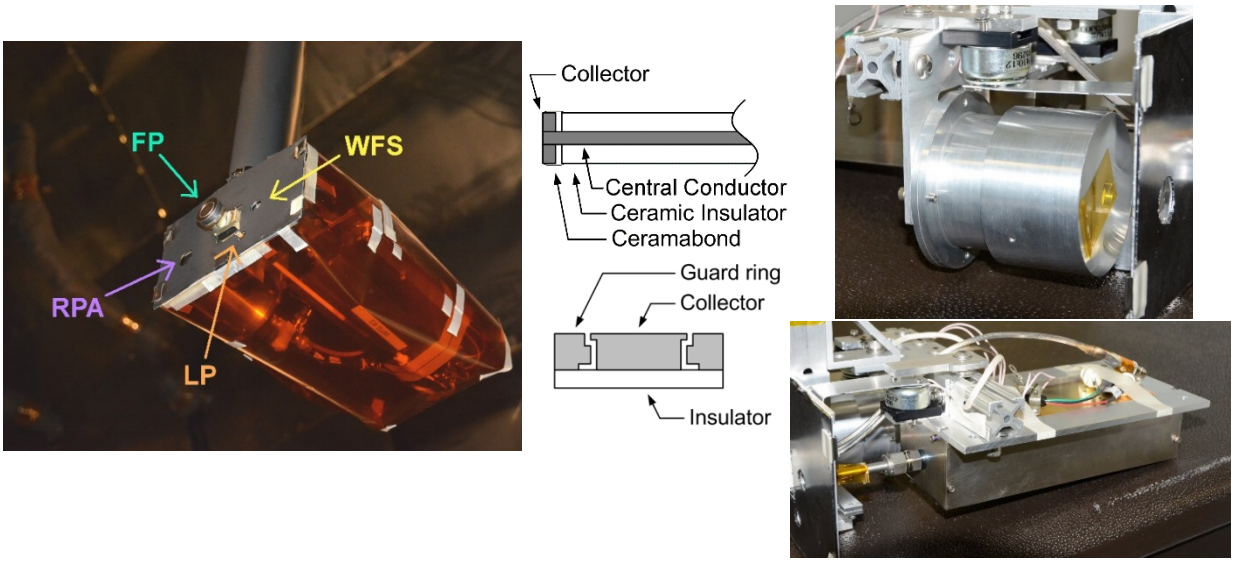

Figure 3. Plasma probe package (left), cross section of Langmuir probe (center top) and Faraday probe (center bottom), photograph of RPA (right top), and photograph of WFS (right bottom).

The FP was of GRC design[29,30] and was used to measure ion current density in the farfield plume. The collector and guard ring were made of molybdenum and the insulating back was made of Macor. Angular resolution of the FP data was ~0.5°. At each operating condition, the FP was azimuthally swept at five different distances, 4.2, 5.2, 6.1, 7.0, and 7.9 mean channel diameter (MCD). An additional sweep at 7.9 MCD was conducted to make sure the data was not dependent on the sweep direction. During testing, measurements were made at different bias voltages in increments of 10V. The results indicated that -30V bias with respect to facility ground was sufficient to repel incoming electrons for all operating conditions.

The LP consisted of a single tungsten wire protruding from an alumina tube. This probe was used to obtain the local plasma potential so that the RPA data can be corrected by this potential. The LP was swept at 3Hz for 1sec at each location. FP and LP data were measured by a data acquisition device. Figure 3 (center) shows cross-sectional diagrams of the FP (bottom center) and LP (top center).

The RPA was of AFRL design.[29,30] During testing, the electron suppression and repelling grids were biased to -30V with respect to facility ground while the ion retarding grid voltage was swept. The ion retarding grid was biased by a sourcemeter while the collected current was measured by a picoammeter. Data were taken at polar angles of ±100°, ±95°, ±90°, ±85°, ±80°, ±75°, ±70°, ±65°, ±60°, ±55°, ±50°, ±45°, ±40°, ±35°, ±30°, ±15°, and 0°. Figure 3 (top right) shows a photograph of the RPA.

The WFS was a commercial product and was used to measure charged species current fractions. The WFS was the product from a Small Business Innovation Research contract and has a prior history of usage.[29,30,31] The electron suppression plate was biased at -30V with respect to facility ground to suppress secondary electron emission (SEE) from the collector. The main bias plate voltage was swept by a picoammeter, which also measured the collector current. Data was taken at 0°. Figure 3 (bottom right) shows a photograph of the WFS.

The experiment was conducted via a LabVIEW program from a dedicated data acquisition computer. The computer interfaced with the motion stages via a set of motion controllers. The computer also directly interfaced with the data acquisition device, picoammeters, and sourcemeter. During the experiment, the computer automatically activated the various motion stages, shutters, and probes in the proper sequence.

3. Time Resolved Thruster Telemetry

The temporal behavior of the TDU-3 Hall thruster key parameters were continuously monitored by multiple oscilloscopes. The oscilloscope telemetry included both AC and DC monitoring of the thruster discharge current and voltage, thruster body voltage and current, cathode-to-ground voltage, and other key cathode parameters. The internal functionality of the oscilloscopes was used to calculate the RMS, Pk2Pk, and mean value where appropriate. The oscilloscope telemetry was recorded using the data acquisition system on the same time scale as the other telemetry. The logging of the thruster temporal characteristics provided additional information on the high-speed IVB sweep that

was useful when analyzing the thruster stability. Additionally, a dedicated oscilloscope was used to record five million points of data on the discharge current and voltage for generation of PSD plots at selected thruster operating conditions.

IV. TDU-3 Performance Evaluation Results

The TDU-3 thruster performance was characterized at different thruster operating conditions that included:

A. Performance at discharge voltages between 300V and 600V including tests at the reference firing conditions (RFCs);
B. Thruster magnetic mapping at discharge voltages of 300V-600V;
C. Cathode flow fraction (CFF) variation tests;
D. Harness inductance variation tests;
E. RFCs for reverse magnet polarity; and
F. Thruster discharge current excursion tests.

A. Reference Firing Conditions

The thruster performance was measured at thruster discharge voltages between 300V and 600V in increments of 100V. For a given discharge voltage setting, the thruster's discharge current was varied between 5A and 20A in increments of 5A. Tests were also performed at the thruster's RFCs listed in Table 1. During thruster performance characterization a cathode flow fraction of 7% was implemented and tests were performed at the thruster's nominal normalized magnetic field setting of 1.6.

Table 1. Summary of TDU-1 and TDU-3 performance at the RFCs.

	TDU-3 Boron Nitride Silica Composite				TDU-1 Heritage Boron Nitride			
	Anode Flow, mg/s	Thrust, mN	Thrust Efficiency, %	Isp, sec	Anode Flow, mg/s	Thrust, mN	Thrust Efficiency, %	Isp, sec
300V 6.25 kW	19.21	389	58.0	1930	19.14	392	59.9	1950
400V 8.33 kW	19.68	472	62.9	2288	19.64	478	65.1	2317
500V 10.4 kW	20.05	538	64.3	2558	19.94	542	66.3	2594
600V 12.5 kW	20.64	603	65.4	2784	20.62	611	67.7	2826
600V 12.5 kW High Br	20.48	604	66.0	2810	20.24	612	69.4	2883

Table 1 presents a comparison of the TDU-1 and TDU-3 thruster performance. Table 1 indicates that TDU-1 performance (w/ heritage BN) is slightly higher than that of TDU-3 (W/ BN silica composite), but that difference is within the accuracy of the thrust measurement; as such the measurements are considered in family.

Figure 4 presents the anode mass flow rate as function of discharge power for discharge voltages between 300V and 600V. Linear fits can be applied to the plot and they indicate that that the slope of the ma/Id decreases as the discharge voltage is increased, which is similar to other Hall thrusters.

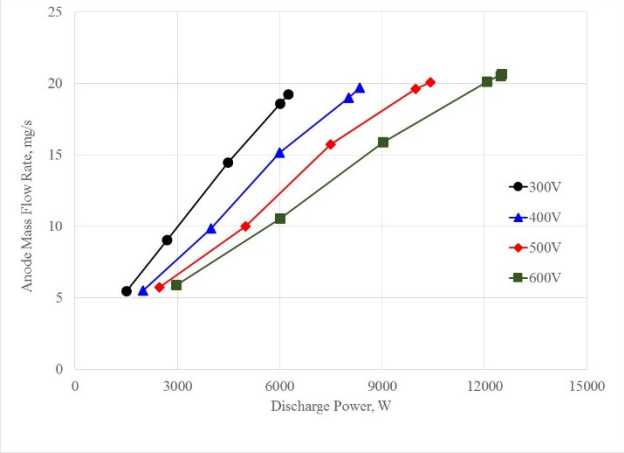

Figure **4. TDU-3 anode flow rate variation for discharge voltage operation of 300V, 400V, 500V, and 600V.**

Figure 5 presents the thrust efficiency as a function of discharge power. Similar to the TDU-1 and TDU-2 thrusters,[13,32] performance improves with increased thruster power at all the operating discharge voltages due to the increase in current density. A peak thrust efficiency of 65% is achieved at a discharge power of 12.5kW at a discharge voltage of 600V. Figure 6 presents the specific impulse as a function of discharge power. At 12.5kW and at a discharge voltage of 600V a specific impulse of 2,800sec is attained.

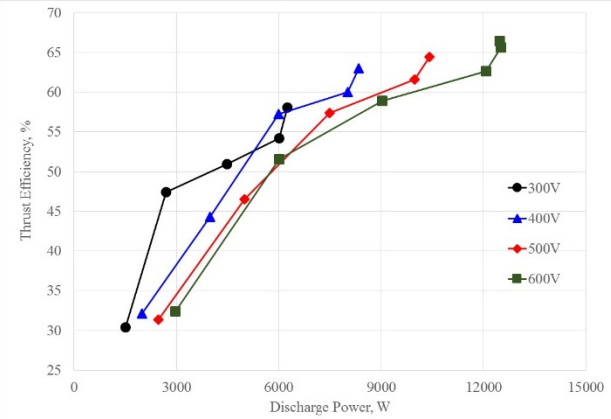

Figure **5. TDU-3 thrust efficiency variation for discharge voltage operation of 300V, 400V, 500V, and 600V.**

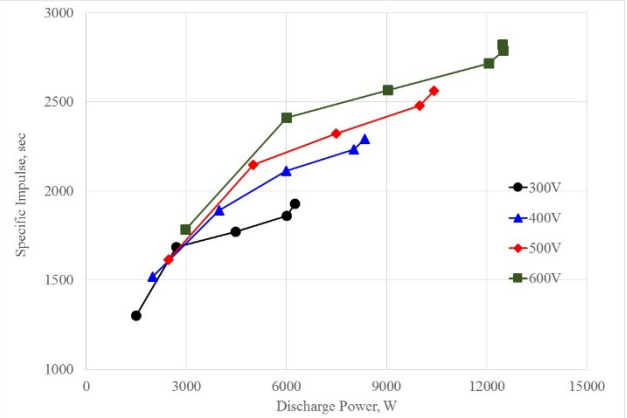

Figure **6. TDU-3 specific impulse variation for discharge voltage operation of 300V, 400V, 500V, and 600V.**

B. Magnet Mapping

The thruster performance was mapped at the RFCs at varying magnetic field strength. This was performed to assess thruster performance at various magnetic field settings to characterize the thruster's magnetic field operating range. The test procedure included varying the peak radial magnetic field strength along the discharge channel center line (by varying the inner and outer electromagnet currents). After adjusting the magnetic field strength the anode and cathode flow rates (to maintain 7% flow fraction) were adjusted to maintain the nominal thruster discharge current magnitude at that operating point. The magnetic field magnitudes reported in this paper are reported as normalized values.

Figure 7 presents the anode flow rate variation with increased magnetic field strength. For thruster operation at 300V to 500V the anode flow rate dropped as the magnetic field strength was increased, this is similar to results presented for TDU-1. At 600V, the anode flow rate almost maintained a constant profile as the magnetic field strength was varied.

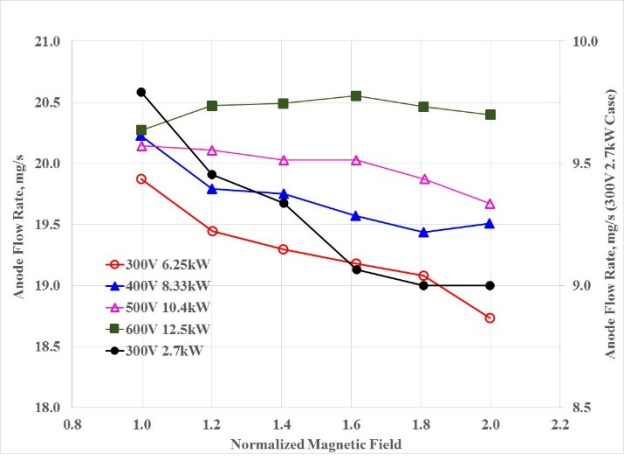

Figure **7. TDU-3 anode flow rates for thruster operation at the RFCs as a function of the normalized magnetic field magnitude.**

Figure 8 presents the thrust efficiency as a function of normalized magnetic field strength. Results in Fig. 8 show that, for the most part, that thruster efficiency increased slightly with increased field length or maintained a somewhat flat profile. This is important because, for the TDU-3 thruster, a normalized magnetic field strength 1.6 was chosen as the nominal thruster magnetic field settings, which would allow for substantial magnetic field margin less and greater than the nominal set point. This results in flexibility with the magnetic field setting if required. Figure 9 presents the thruster specific impulse variation with magnetic field strength, which show a nearly flat profile for the specific impulse variation with magnetic field.

In conclusion, the TDU-3 magnetic field mapping results indicated that the selection of 1.6 as the nominal magnetic field setting for TDU-3 operation does results in acceptable thruster performance with considerable magnetic field range. That range may be needed to optimize thruster performance and stability during space operation.

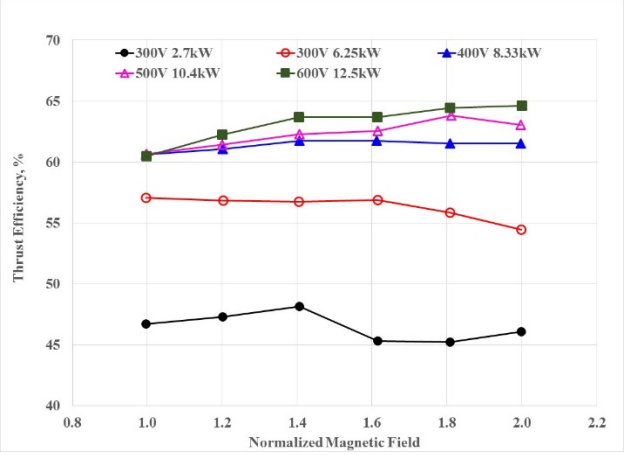

Figure 8. TDU-3 thrust efficiency magnitudes for thruster operation at the RFCs as a function of the normalized magnetic field magnitude.

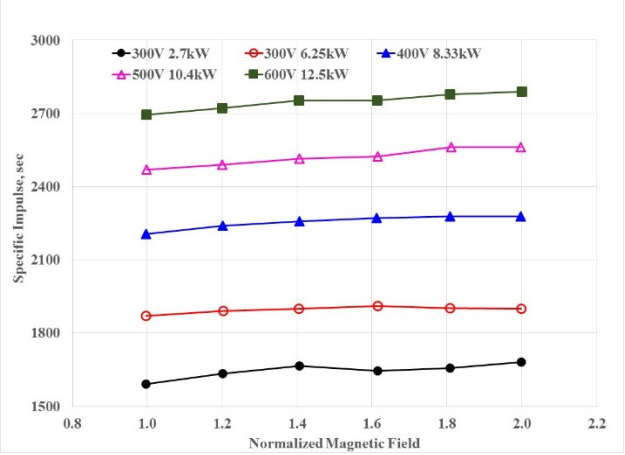

Figure 9. TDU-3 specific impulse magnitudes for thruster operation at the RFCs as a function of the normalized magnetic field magnitude.

C. Cathode Flow Fraction

The thruster performance was assessed at the RFCs operating throttle points for varying CFF. The CFF was varied between 5 and 9% at 1% increments. Figure 10 presents thrust efficiency as a function of CFF. Results in Fig.10 indicate that the thrust efficiency increases slightly or remains constant as the cathode flow rate is increased. Figure 11 presents the specific impulse as a function of the CFF. Results in Fig.11 also indicate that the specific impulse did not vary much with CFF, this indicates that the reduction in the cathode flow was accompanied by a reduction in the thrust magnitude resulting in an almost constant specific impulse.

Figure 12 presents the cathode-to-ground voltage as a function of CFF. For all test conditions increasing the cathode flow rate resulted in a lower cathode coupling voltage, this nominal behavior is attributed to improved coupling between the cathode and the thruster. Figure 13 presents the thruster body current as a function of the CFF. AT a given operating point, the body current increases with increased CFF, it is postulated that the cathode emission current increased due to higher ionization as a result of the higher cathode flow. Also results in Fig. 13 show that thruster operation at higher discharge voltage results in increased thruster body current, this is attributed to the fact that at higher discharge voltages the thruster's plume electron temperature is higher resulting in higher ionization rates and more current collected by the thruster. Finally, comparing the thruster body current for nominal and high magnetic field operation at 600V, also indicates that the thruster body current is almost 20% larger at high magnetic field strength when compared to nominal magnetic field strength. This is attributed to the fact at higher field strength cross field diffusion is reduced and that translates into more ions being trapped by the thruster's magnetic field lines which wrap back to the thruster body.

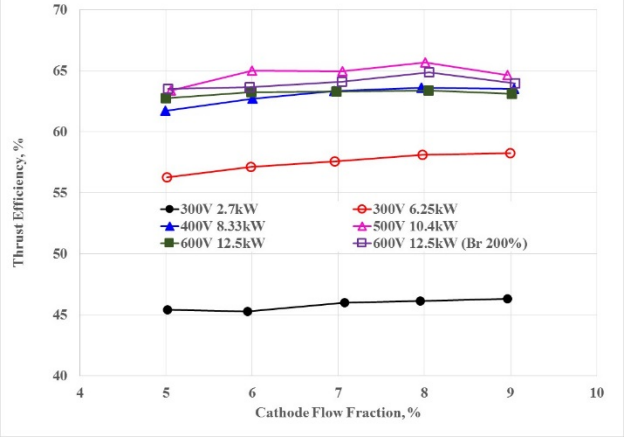

Figure 10. TDU-3 thrust efficiency magnitudes for thruster operation at the RFCs as a function of the cathode flow fraction (CFF).

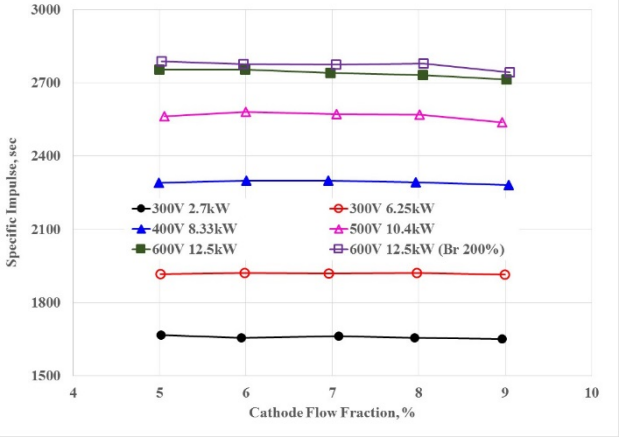

Figure 11. TDU-3 specific impulse magnitudes for thruster operation at the RFCs as a function of the cathode flow fraction (CFF).

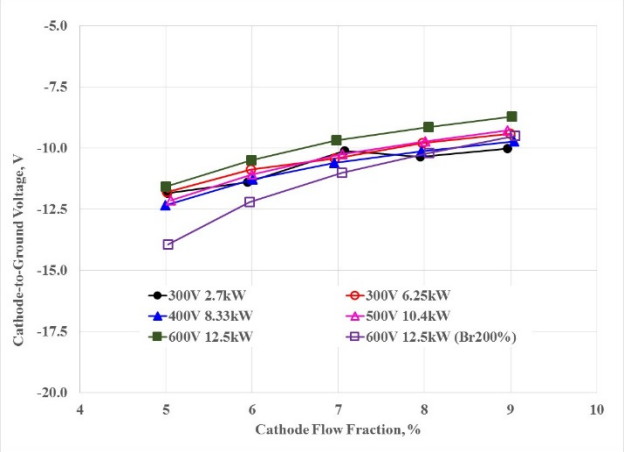

Figure 12. TDU-3 cathode-to-ground voltage magnitudes for thruster operation at the RFCs as a function of the cathode flow fraction (CFF).

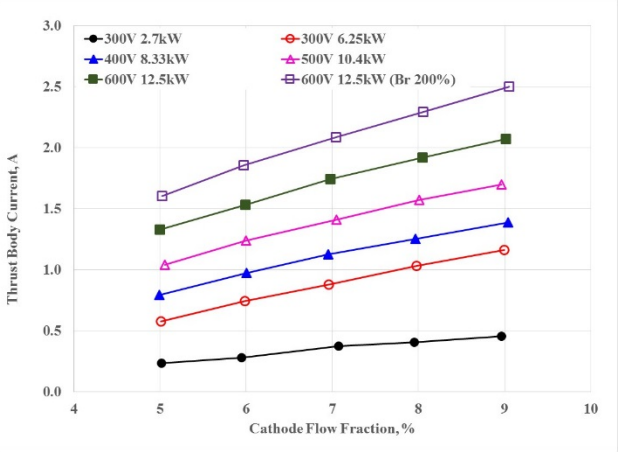

Figure 13. TDU-3 thruster body current magnitudes for thruster operation at the RFCs as a function of the cathode flow fraction (CFF).

D. Harness Inductance Test

Testing was performed at three additional harness inductance magnitudes at two thruster operating throttle points: 300V/6.25kW and 600V/12.5kW. A companion paper provide more details about the approach the HERMeS thruster team undertook in designing the test harness for the HERMeS thruster testing at NASA GRC.[33] The tests were performed to evaluate the impact of changing the harness inductance on the thruster performance and stability. The nominal line inductance during the test was ~3.4 μH. Testing was performed at three additional values of 2.8 μH (by removing tuning inductor), 17.8 μH, and 32.8 μH. Figures 14 and 15 present the thrust efficiency and specific impulse magnitudes, respectively, as a function of the harness inductance. Results in Figs. 14 and 15 indicate, that for the most part, the variation in thrust efficiency and specific impulse was within ~1%, increasing the harness inductance by a factor of 10x did not alter the thruster performance although the discharge voltage oscillations Pk2Pk increased to 182 V from their nominal 30 V.

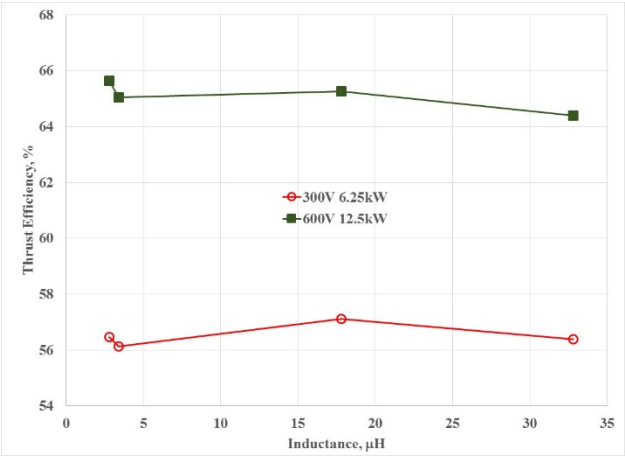

Figure 14. TDU-3 thrust efficiency magnitudes for thruster operation at the 300V/6.25 kW and 600V/12.5 kW as a function of harness inductance.

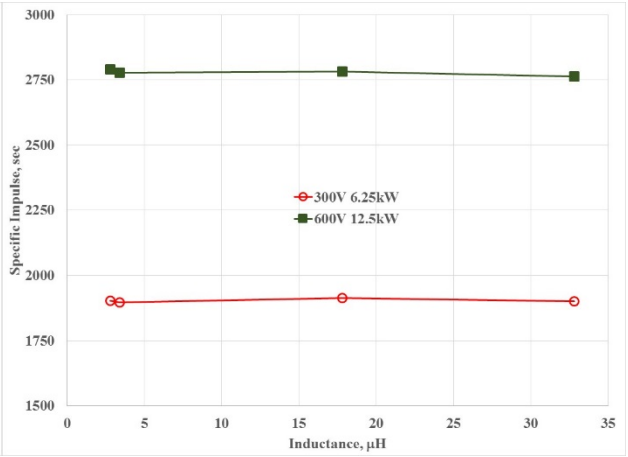

Figure 15. TDU-3 specific impulse magnitudes for thruster operation at the 300V/6.25 kW and 600V/12.5 kW as a function of harness inductance.

E. Reverse Polarity Test

Tests of the TDU-3 thruster were performed using reverse magnet polarity. That was achieved by reversing the magnet current direction on the inner and outer electromagnets and assessing thruster performance at the RFCs. Table 2 presents a summary of the thruster mass flow rate and performance for nominal and reverse polarity thruster operation. While the anode flow rate was almost identical for all operating conditions, the thrust magnitude for reverse polarity operation was lower than for nominal polarity operation. At 300V/6.25 kW the thrust level for reverse polarity operation was ~5% lower than the thrust produced with nominal polarity operation. At 600V/12.5 kW the thrust level for reverse polarity operation was 2% lower than for nominal operation. The decrease in thrust levels for the reverse electromagnet polarity in unknown but additional investigation will be performed to re-evaluate the thruster performance when the radial magnetic field direction is reversed.

Table 2. Comparison of TDU-3 thruster performance with nominal and reverse magnet settings.

	Nominal Polarity				Reverse Polarity			
	Anode Flow, mg/s	Thrust, mN	Thrust Efficiency, %	Isp, sec	Anode Flow, mg/s	Thrust, mN	Thrust Efficiency, %	Isp, sec
300V 6.25 kW	19.21	389	58.0	1930	19.22	370	52.5	1830
400V 8.33 kW	19.68	472	62.9	2288	19.62	452	57.9	2200
500V 10.4 kW	20.05	538	64.3	2558	19.99	518	59.9	2470
600V 12.5 kW	20.64	603	65.4	2784	20.61	585	61.6	2700
600V 12.5 kW High Br	20.48	604	66.0	2810	20.45	590	63.0	2750

F. Discharge Current Excursion Test

The thruster performance was evaluated at ±1 A from the nominal operating current of 20.8A and discharge voltage was varied between 300V and 600V at 25V increments. Testing was performed at the nominal magnetic field setting and for a CFF of 7%. Tests were performed to obtain more refined thruster performance values for mission analysis. Tests results found that the thruster maintained its performance levels and operated in a steady manner. Figures 16 and 17 present the thrust efficiency and specific impulse magnitudes for the discharge current excursion test. In general, it is observed that higher thrust performance (thrust efficiency and specific impulse) was obtained at higher current for a given discharge voltage setting.

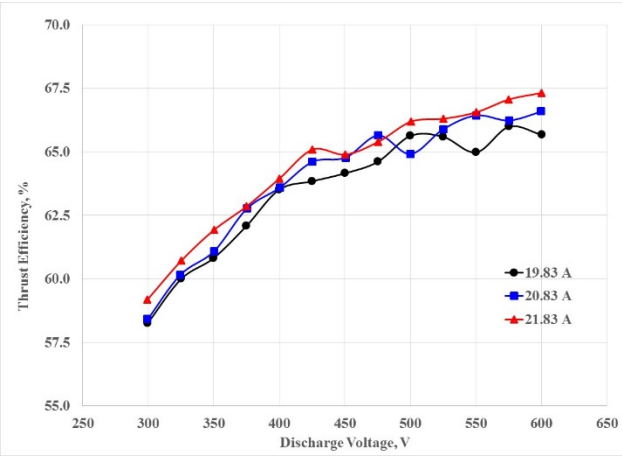

Figure 16. TDU-3 thrust efficiency for thruster operation at 19.8, 20.8, and 21.8A as a function of discharge voltages between 300 and 600V.

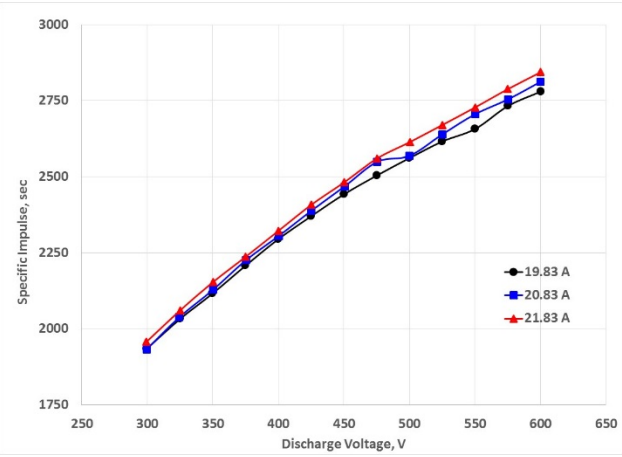

Figure 17. TDU-3 specific impulse for thruster operation at 19.8, 20.8, and 21.8A as a function of discharge voltages between 300 and 600V.

V.TDU-3 Stability Characterization Results

This section presents an assessment of the TDU-3 stability. To characterize the TDU-3 thruster stability, high speed measurements of discharge current oscillations were performed. The discharge current Pk2Pk and RMS were

used to provide an assessment of the thruster stability.[34,35] In addition, PSD analysis was performed on the discharge current waveforms for selected operating conditions. The discharge current waveforms were analyzed to determine the dominant breathing mode frequency and to further elucidate the mode transitions during thruster operation. Finally, the IVB maps of the thruster operation were performed at selected flow rates.

The TDU-3 thruster oscillations were characterized at different thruster operating conditions that included:

A. Performance at discharge voltages between 300V and 600V including tests at the RFCs;
B. Thruster magnetic mapping at discharge voltages between 300 and 600V;
C. Cathode flow fraction variation tests;
D. Harness inductance variation tests; and
E. RFCs for reverse magnet polarity;

A. Reference Firing Conditions

The discharge current Pk2Pk and RMS magnitudes for the discharge current waveforms are presented in Figs. 18 and 19. Results in Figs. 18 and 19 indicate that for thruster operation at 300V and 400V the discharge oscillations are generally quiescent and that Id Pk2Pk does not exceed 50%. However, as the discharge voltage is increased to 500V the thruster starts to mode hop and transitions to a high oscillatory mode that characterizes its operation at 600V At 500V, the thruster discharge is very oscillatory at 5A then quiets down at 10A and becomes more oscillatory at discharge currents greater than 15 A. At 600V, the thruster discharge is very oscillatory for all operating conditions. Finally it is important to note here that the discharge current Pk2Pk and RMS values for tDU-12 and TDU-3 at the RFCs were very similar and that the discharge channel grade material did not affect the thruster's stability, as is presented in Table 3.

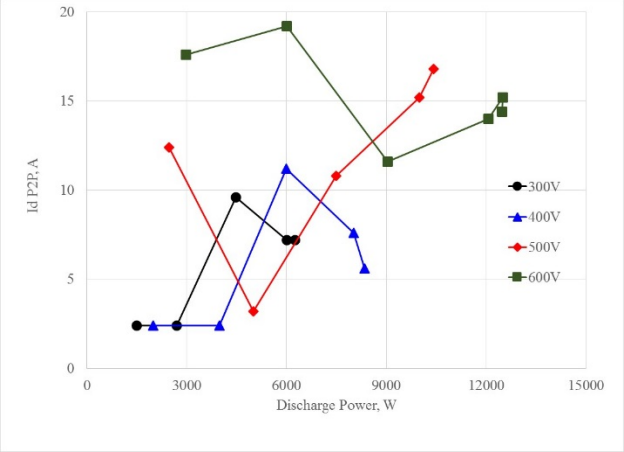

Figure 18. TDU-3 discharge current Pk2Pk as a function of discharge power for thruster operation at discharge voltages of 300, 400, 500, and 600V for nominal magnetic field setting.

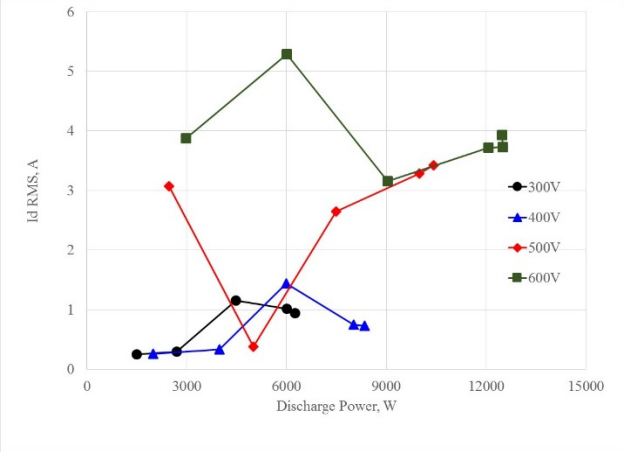

Figure 19. TDU-3 discharge current RMS as a function of discharge power for thruster operation at discharge voltages of 300, 400, 500, and 600V for nominal magnetic field setting.

Table 3: Summary of TDU-2 and TDU-1 discharge current and voltage Pk2Pk and RMS magnitudes at the RFCs

	TDU-3 Boron Nitride Silica Composite				TDU-1 Heritage Boron Nitride			
	Id Pk2Pk	Id RMS	Vd Pk2Pk	Vd RMS	Id Pk2Pk	Id RMS	Vd Pk2Pk	Vd RMS
300V 6.25 kW	8	0.95	11.6	1.47	4.6	0.65	6.4	0.84
400V 8.33 kW	5.6	0.73	11.2	1.25	4.8	0.65	7.4	0.92
500V 10.4 kW	16.8	3.42	24	2.59	16.8	3.78	15	1.84
600V 12.5 kW	15.6	3.73	26.4	3.22	15.8	3.98	19	2.68
600V 12.5 kW High Br	14.4	3.93	26	3.5	13	3.70	17.8	2.57

B. Magnet Mapping

The discharge current Pk2Pk and RMS magnitudes for the discharge current waveforms are presented in Figs. 20 and 21 for the magnet mapping tests. Results are presented for thruster operation at the RFCs. At 300V/2.7kW the thruster oscillation levels decreased with increased magnetic field strength. At 300V/6.25kW the oscillation levels decreased initially with increased magnetic field strength but then started to increase at the nominal field setting of 1.6. At 400V/8.3kW the oscillation levels increased slightly with increased field strength and then decreased at the nominal field setting and beyond. Finally, at 500V/10.4 kW and 600V/12.5 kW the lowest oscillation levels are attained at the lowest magnetic field setting but then drastically increased as the field strength is increased and then remained relatively constant.

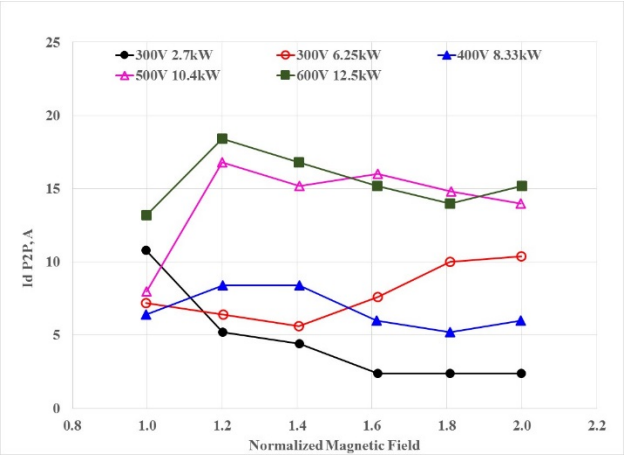

Figure 20. TDU-3 discharge current Pk2Pk at the RFCs as a function of normalized magnetic field.

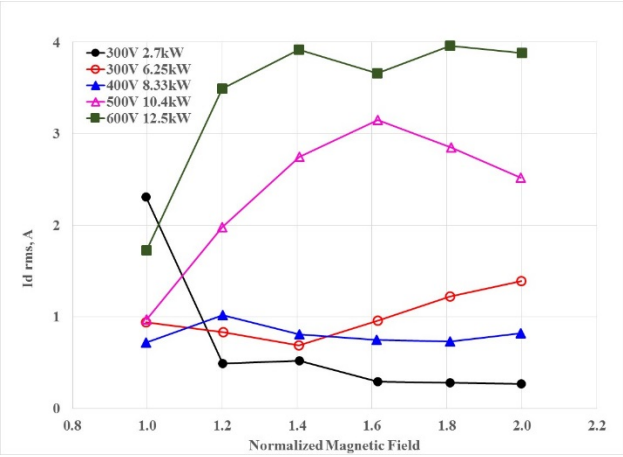

Figure 21. TDU-3 discharge current RMS at the RFCs as a function of normalized magnetic field.

Figure 22 presents the PSDs for the 300V/2.7 kW operating point. At the lowest field setting the dominant thruster frequency is ~17 kHz, but as the field strength is increased it becomes lower and another peak in the PSDs starts to emerge at ~60Hz. It is speculated that further increases in the magnetic field strength may result in a more oscillatory discharge that may hop to another mode. Figure 23 presents the PSDs for the 300V/6.25kW operating point. The PSDs in Fig. 23 indicate that at low field strength two dominant frequencies exist at ~10 kHz and 72 kHz, increasing the field results in reduced energy at the higher frequency and the lower frequency oscillations becoming more dominant as is evident by the discharge oscillation levels at the highest field strength. Figure 24 presents the PSDs for the 400V/8.3kW operating point. The PSDs in Fig. 24 show that as the magnetic field strength is increased the PSD magnitude at ~10 kHz decreases and the PSD magnitude at ~70 kHz increases but both magnitudes still indicate low oscillation levels. It is worth noting here that thruster operation at 400V/8.3kW is the most quiescent thruster operating point. Figure 25 presents the PSD at 500V/10.4kW. As was shown in Figs 20 and 21, the thruster operation is characterized by low oscillation levels at the lowest magnetic field settings but grow substantially as the field strength is increased. This behavior can also be seen in Fig. 25. At the lowest field setting the PSD levels are low, as soon as the field strength is increased to 1.2 and above, the dominant frequency starts to shift from ~15kHz to higher values along with a marked increase in the amplitude of the PSD. This correlates well with the results in Figs. 20 and 21. Figure 26 presents the PSD at 600V/12.5kW. As was shown in Figs 20 and 21, the thruster operation is characterized by lower oscillations at the lowest magnetic field settings but they start to grow as the field strength is increased, which can also be seen in Fig. 26. At the lowest field setting the PSD levels are lower than other field settings, as soon as the field strength is increased to 1.2 and above, the dominant frequency starts to shift from ~10kHz to higher values along with a marked increase in the amplitude of the PSD at all frequency levels. This correlates well with the results in Figs. 20 and 21. What is also interesting about the PSDs for the 600V/12.5kW operating conditions is the emergence of relatively strong oscillations at higher frequencies of 100kHz and 160kHz, which may be associated with cathode operation.[36]

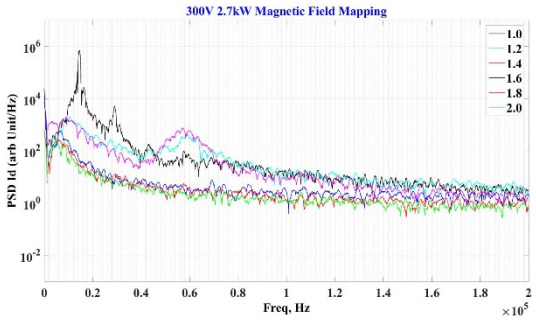

Figure 22. TDU-3 PSD profiles for thruster operation at 300V/2.7kW as a function of the normalized magnetic field.

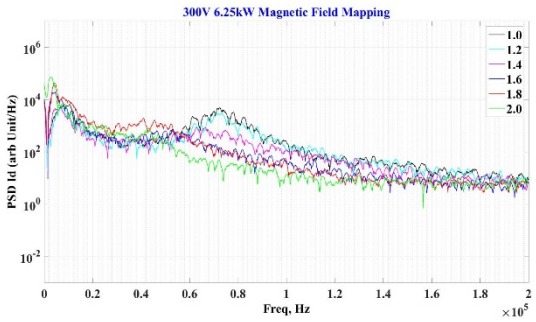

Figure 23. TDU-3 PSD profiles for thruster operation at 300V/6.25kW as a function of the normalized magnetic field.

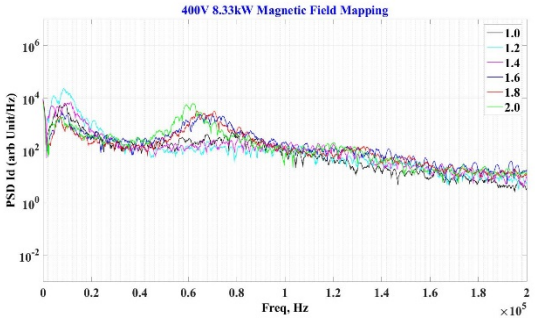

Figure 24. TDU-3 PSD profiles for thruster operation at 400V/8.3kW as a function of the normalized magnetic field.

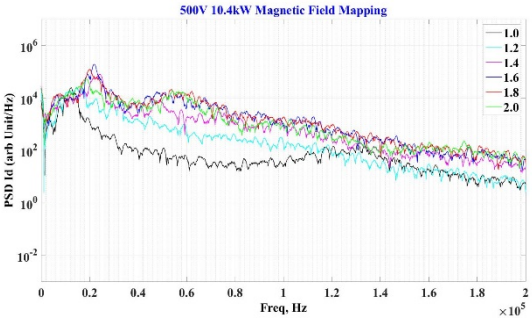

Figure 25. TDU-3 PSD profiles for thruster operation at 500V/10.4kW as a function of the normalized magnetic field.

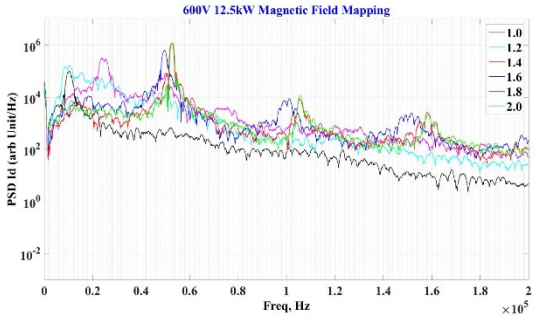

Figure 26. TDU-3 PSD profiles for thruster operation at 600V/12.5kW as a function of the normalized magnetic field.

C. Cathode Flow Fraction

The discharge current Pk2Pk and RMS magnitudes for the discharge current waveforms are presented in Figs. 27 and 28 for the CFF tests. In general results in Figs. 27 and 28 indicate that the thruster discharge current oscillation levels increased slightly with increased CFF and the increase was modest. The PSDs for the CFF tests are presented in Figs. 29, 30, 31, 32, 33, and 34 for thruster operation at 300V/2.7kW, 300V/6.25kW, 400V/8.3kW, 500V/10.4kW, 600V/12.5kW, and 600V/12.5 kW high Br, respectively. Results in Figs. 29-34 indicate that the thruster operating mode remained unchanged as the CFF was varied and that the oscillation levels only increased slightly with increased CFF. The above results indicate that thruster operation at a CFF of 5% is stable but a a cost of lower thruster performance as was shown in Figs 10 and 11.

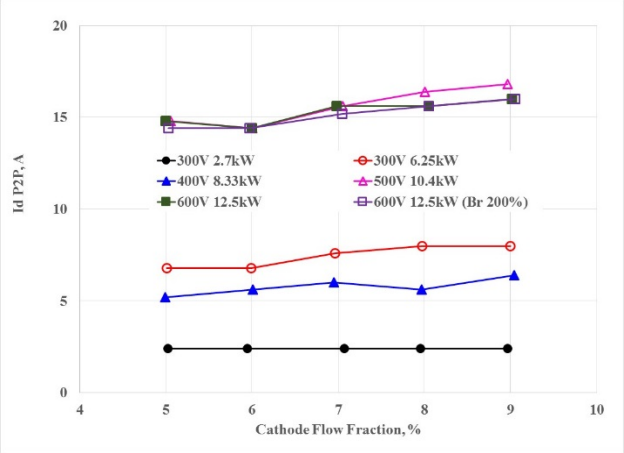

Figure 27. TDU-3 discharge current Pk2Pk profiles for thruster operation at RFCs as a function of the CFF.

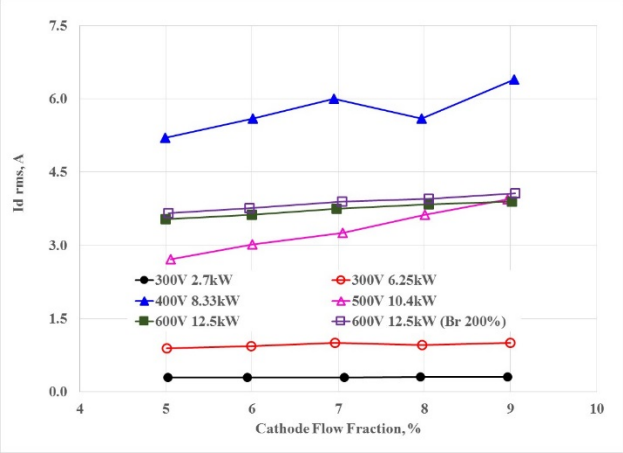

Figure 28. TDU-3 discharge current RMS profiles for thruster operation at RFCs as a function of the CFF.

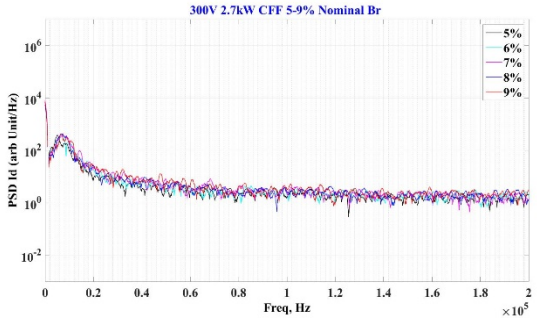

Figure 29. TDU-3 discharge current PSD profiles at 300V/2.7kW operating point as a function of the CFF.

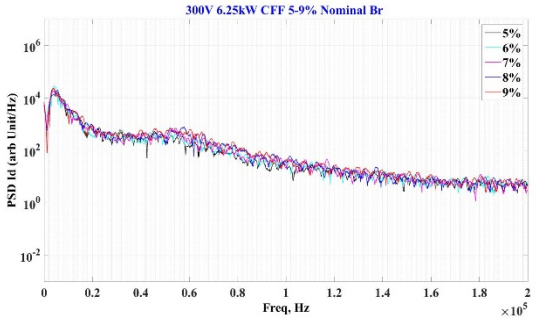

Figure 30. TDU-3 discharge current PSD profiles at 300V/6.25kW operating point as a function of the CFF.

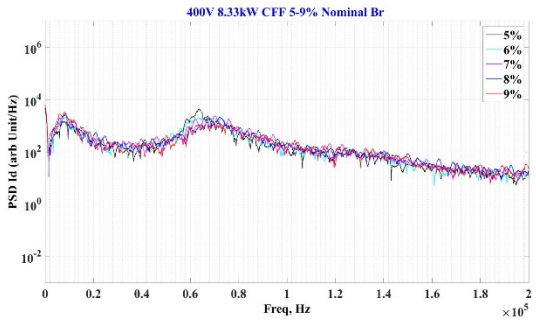

Figure 31. TDU-3 discharge current PSD profiles at 400V/8.3kW operating point as a function of the CFF.

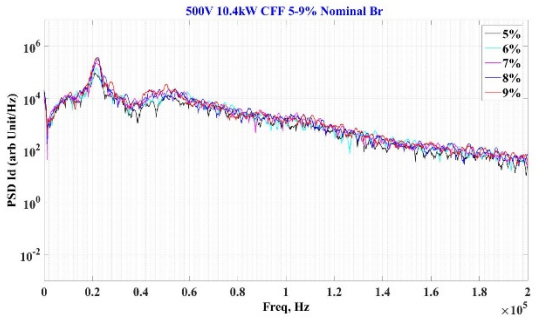

Figure 32. TDU-3 discharge current PSD profiles at 500V/10.4kW operating point as a function of the CFF.

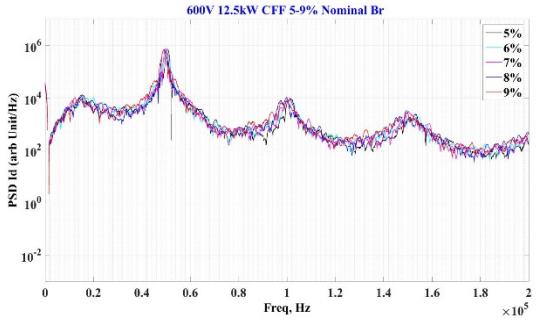

Figure 33. TDU-3 discharge current PSD profiles at 600V/12.5kW operating point as a function of the CFF.

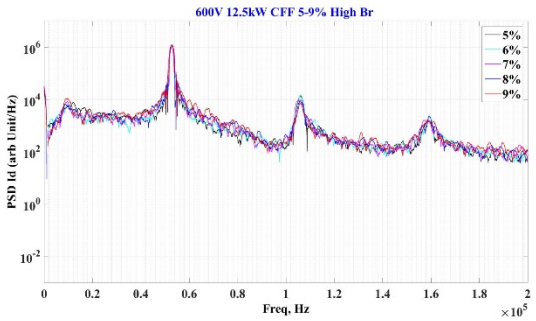

Figure 34. TDU-3 discharge current PSD profiles at 600V/12.5kW high Br operating point as a function of the CFF.

D. Harness Inductance test

The discharge voltage Pk2Pk and RMS for the thruster sense discharge voltage are presented in Figs 35 and 36, respectively. The thruster's sense discharge voltage was measured at the thruster's power terminals and a low inductance cable was routed through the thrust stand waterfall to transmit the measurement for recording by high speed differential probes outside VF-5. Results in Figs. 35 and 36 show that increased harness inductance resulted in increased discharge voltage oscillation magnitudes, as was expected.[33] At the 600V/12.5 kW operating point and at the nominal harness inductance of 3.4μH, the discharge voltage Pk2Pk and RMS magnitude were 30V and 3.8V, respectively. When the harness inductance was changed to 32.8μH, the discharge voltage Pk2Pk and RMS magnitude were 182V and 32V, respectively. The discharge current Pk2Pk and RMS are presented in Figs 37 and 38, respectively. The discharge current oscillation levels did not change as substantially when the harness inductance was varied. This is expected since the thruster oscillation levels are mainly driven by the operating discharge voltage, mass flow rate, and magnetic field setting which determine the plasma characteristics and discharge current oscillations for a given thruster configuration. Results in Fig. 37 and 38 indicate at 300V/6.25kW thruster operating point, varying the thruster's inductance did not result in any change to the discharge current oscillations, which indicates that the thruster continued to operate in the same mode and the discharge was not affected. Whereas, at 600V/12.5kW, the discharge current oscillations only changed when a harness inductance of 32.8μH was implemented. This indicates that the plasma discharge changed as a result of the extreme oscillations in the discharge voltage at that operating point.

Figures 39 and 40 present the discharge voltage PSDs for the thruster operation at 300V/6.25kW and 600V/12.5kW, respectively. Note that Fig. 39 does not include PSD for the 32.8 μH case because that waveform was not saved. The PSD profiles in Figs. 39 and 40 indicate that as the harness inductance was increased so did the power in the PSD profile, which is expected. Figures 41 and 42 present the discharge current PSDs for thruster operation at 300V/6.25kW and 600V/12.5kW, respectively. Results in Fig. 41 indicate that the discharge current PSD did not change for the 300V operation. However, results in Fig.42 indicate that at harness inductance of 32.8μH the PSD

profile varied. This variation occurred due to the very large discharge voltage oscillations (~182V Pk2Pk) that started to impact the thruster operation.

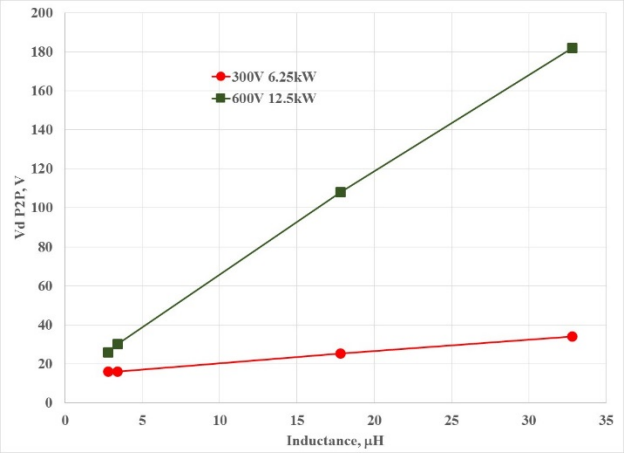

Figure 35. TDU-3 discharge voltage Pk2Pk at 300V/6.25kW and 600V/12.5kW as a function of harness inductance.

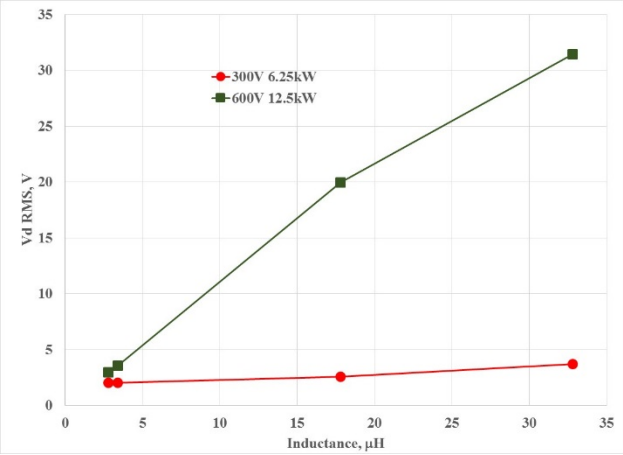

Figure 36. TDU-3 discharge voltage RMS at 300V/6.25kW and 600V/12.5kW as a function of harness inductance.

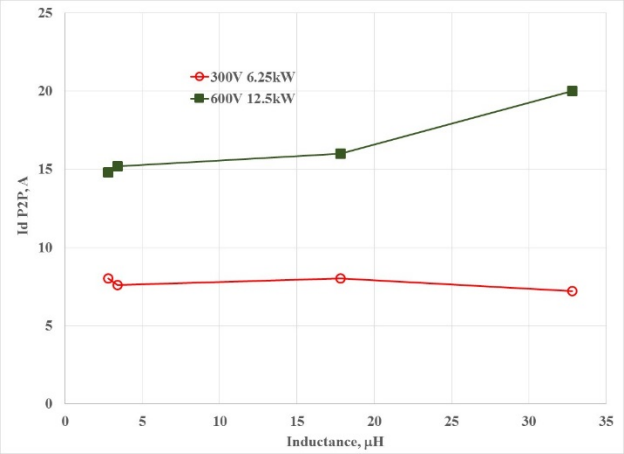

Figure 37. TDU-3 discharge current Pk2Pk at 300V/6.25kW and 600V/12.5kW as a function of harness inductance.

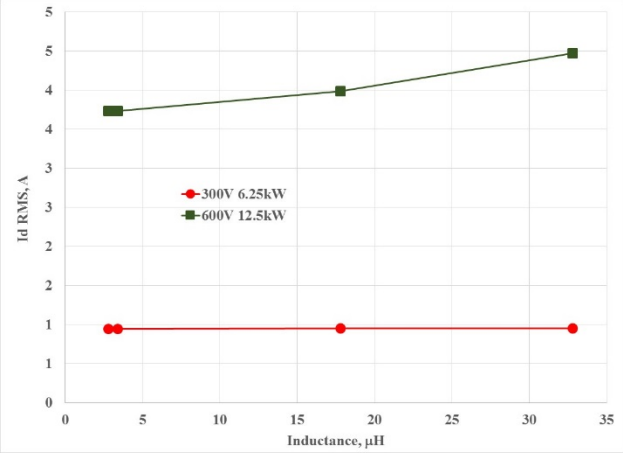

Figure 38. TDU-3 discharge current RMS at 300V/6.25kW and 600V/12.5kW as a function of harness inductance.

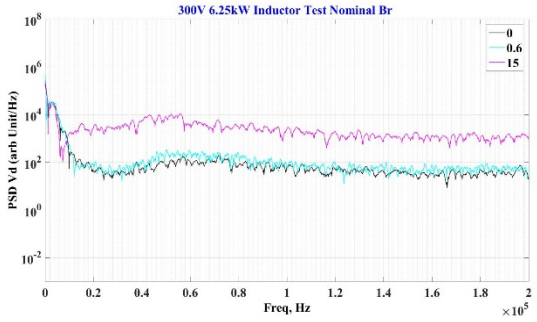

Figure 39. TDU-3 discharge voltage PSDs at 300V/6.25kW as a function of harness inductance.

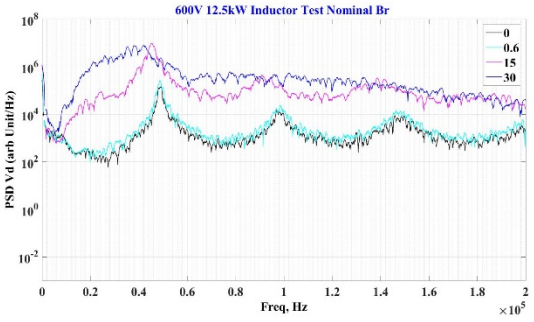

Figure 40. TDU-3 discharge voltage PSDs at 600V/12.5kW as a function of harness inductance.

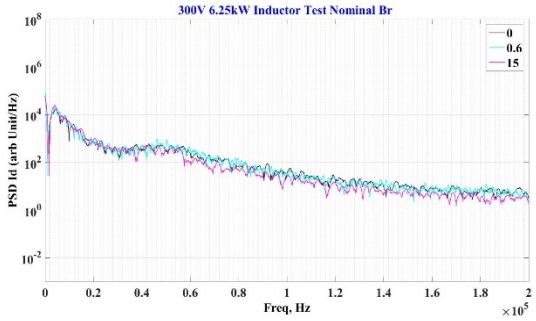

Figure 41. TDU-3 discharge current PSDs at 300V/6.25kW as a function of harness inductance.

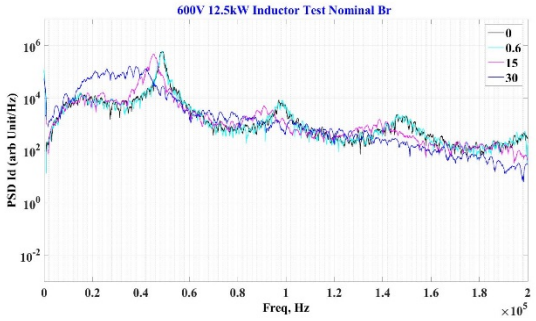

Figure 42. TDU-3 discharge current PSDs at 600V/12.5kW as a function of harness inductance.

E. Reverse Polarity Test

Table 4 presents the discharge current Pk2Pk and RMS comparison between the nominal and reverse polarity tests. Results in Table 4 indicate that the thruster discharge current oscillations levels were very similar for the two tests and did not vary appreciably. This was an expected finding but it has to be reconciled with the fact that the thruster's performance changed considerably when the magnet polarity was reversed (as stated earlier in the paper).

Table 4: Discharge current Pk2Pk and RMS for RFC nominal and reverse polarity operation

	Nominal Polarity		Reverse Polarity	
	Id Pk2Pk, A	Id RMS, A	Id Pk2Pk, A	Id RMS, A
300V 2.7 kW	2.4	0.29	2.4	0.3
300V 6.25 kW	7.2	0.94	8	0.92
400V 8.33 kW	5.6	0.73	6	0.78
500V 10.4 kW	16.8	3.42	15.6	2.93
600V 12.5 kW	15.2	3.73	14.8	3.67
600V 12.5 kW High Br	14.4	3.93	16	3.9

F. Discharge Current Excursion Test

The discharge current Pk2Pk and RMS for the discharge current excursion test are presented in Figures 43 and 44, respectively. The results in Figs. 43 and 44 clearly show that with ±1A discharge current excursion for discharge voltages between 300V and 600V, the thruster continued to operate in a nominal fashion similar to its operation at 20.8A. Additionally, the results presented in Figs. 43 and 44 clearly show that the thruster operates in a quiescent mode up to 400V and then starts to transition to a more oscillatory mode at higher discharge voltages. At discharge voltages above 500 V the thruster operates in a high oscillatory mode as was presented earlier in Figs. 20 and 21.

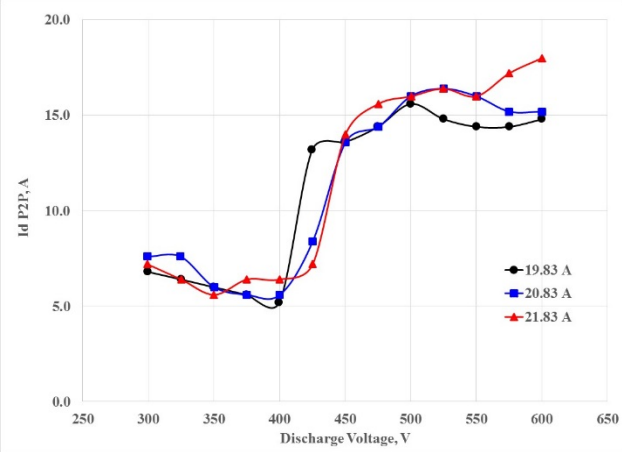

Figure 43. TDU-3 discharge current Pk2Pk 19.8A, 20.8A, and 21.8A as a function of discharge voltage.

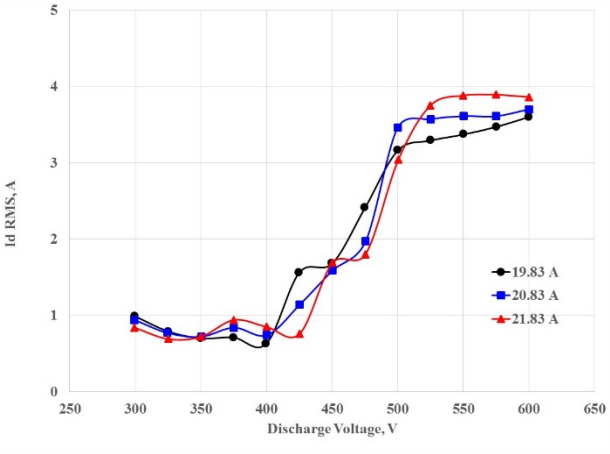

Figure 44. TDU-3 discharge current Pk2Pk 19.8A, 20.8A, and 21.8A as a function of discharge voltage.

G. Current-Voltage-Magnetic Field Maps

Detailed IVB maps were performed during this test sequence. The IVB sweeps were performed by setting the anode and cathode flow rate (typically to 7% of anode flow rate), setting the magnetic field strengths, and then ramping the discharge voltage at increments of 2V every 0.1sec for a selected voltage range. The IVB sweeps were performed at anode flow rates between 6.4mg/sec and 22.5mg/sec. The normalized magnetic field strength was varied between 1 and 2. Table 5 lists the IVB sweep anode flow rates and voltage sweep range. At a flow rate of 20.6mg/s, IVB sweeps were also performed at a CFF of 5% and 9%.

Table 5. TDU-3 IVB sweeps test conditions.

Anode Flow Rate, mg/s	Voltage Sweep Range, V	Cathode Flow Fraction, %
6.4	100-410	7
9.1	100-410	7
15.3	100-610	7
18.4	100-610	7
19.2	100-610	7
20.6	100-610	5
20.6	100-610	7
20.6	100-610	9
22.5	100-510	7

Figure 45 presents the discharge current RMS maps at 6.4mg/s. Results indicate that stable thruster operation can be attained at all magnetic field settings, but the discharge becomes more oscillatory at voltages above 350V for low magnetic field setting. Figure 46 presents the discharge current RMS maps at 9.1mg/s. Results indicate that the discharge is more oscillatory at low magnetic field condition for discharge voltage of 100-150V and 250-400V.

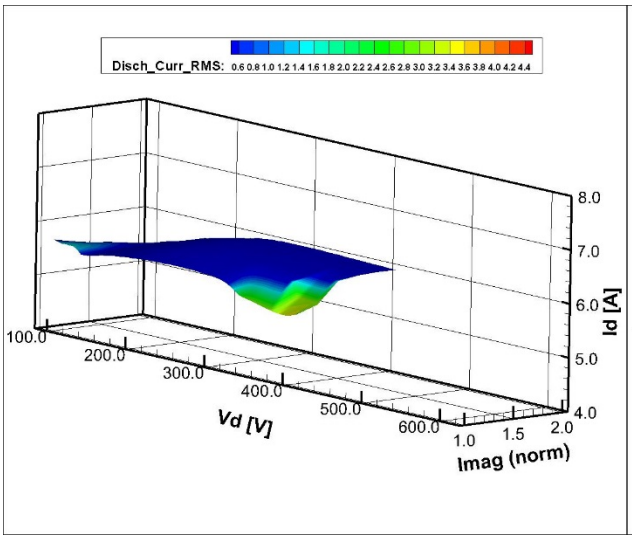

Figure 45. TDU-3 IVB map of discharge current RMS at 6.4mg/s for discharge voltages of 100V to 410V and normalized magnetic field strength of 1 to 2.

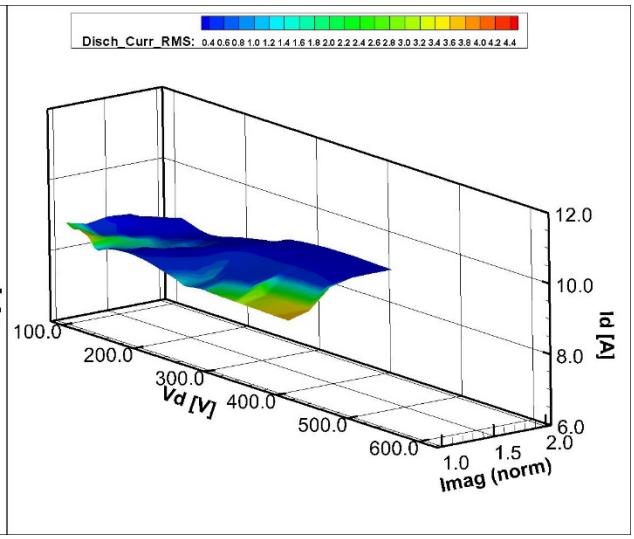

Figure 46. TDU-3 IVB map of discharge current RMS at 9.1mg/s for discharge voltages of 100V to 410V and normalized magnetic field strength of 1 to 2.

Figure 47 presents the discharge current RMS maps at 15.3mg/s. Results indicate that the discharge becomes more oscillatory at discharge voltages above 400 V for all magnetic field settings. Increasing the anode flow to 18.4mg/s and 19.2mg/s yields a similar profiles as is shown in Figs. 48 and 49. The results in Figs. 48 and 49 indicate that the thruster operation is very quiescent for discharge voltage at or below 400 V, but at discharge voltages above 400 V the thruster starts to transition to a more oscillatory mode. Figures 50, 51, and 52 present the IVBs at 20.6 mg/s for CFF of 5%,7%, and 9% respectively. Results in Figs 50-52 indicate that the thruster discharge becomes more oscillatory as the CFF is increased from 5% to 9%. Further investigation will be performed to better understand the cathode mode of operation as the CFF is varied because that will help elucidate how the cathode operational characteristics are impacting the thruster's stability. Additionally, the thruster operation is quiescent at discharge voltages of 400V or below, but as the discharge voltage is increased above 400V, the thruster starts to transition to a higher oscillatory mode. Finally, Fig. 53 presents the discharge current RMS map results for 22.5mg/s. The results in Fig. 53 indicate that the thruster overall operation at that flow rate is characterized by relatively low oscillations.

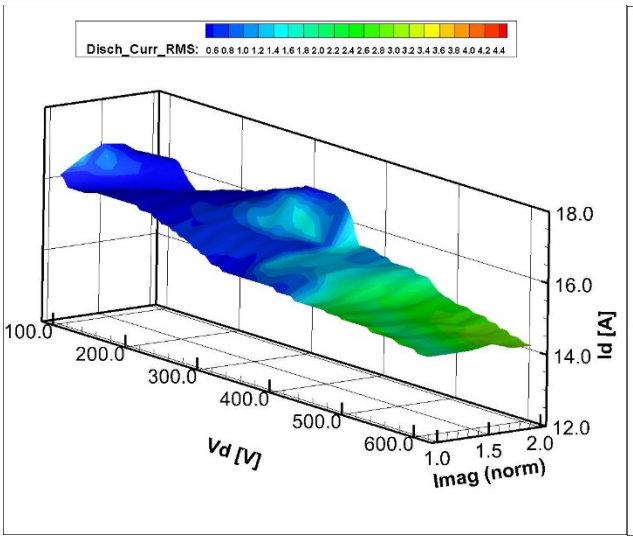

Figure 47. TDU-3 IVB map of discharge current RMS at 15.3mg/s for discharge voltages of 100V to 610V and normalized magnetic field strength of 1 to 2.

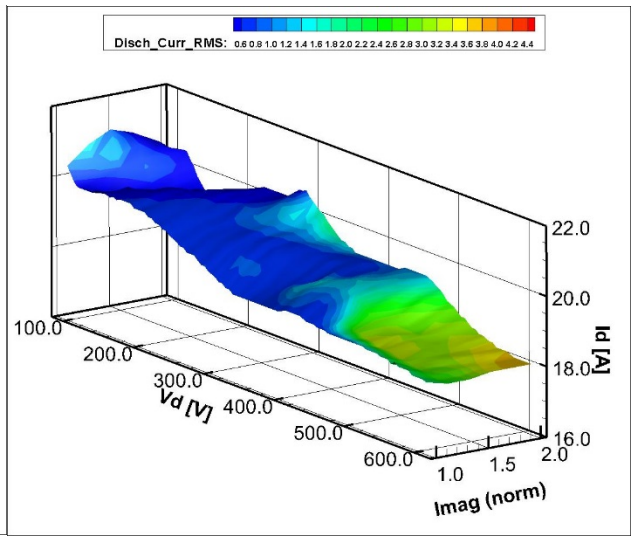

Figure 48. TDU-3 IVB map of discharge current RMS at 18.4mg/s for discharge voltages of 100V to 610V and normalized magnetic field strength of 1 to 2.

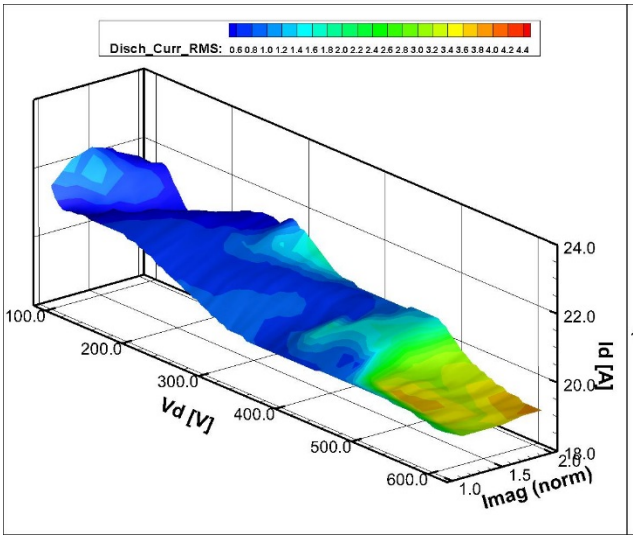

Figure 49. TDU-3 IVB map of discharge current RMS at 19.2mg/s for discharge voltages of 100V to 610V and normalized magnetic field strength of 1 to 2.

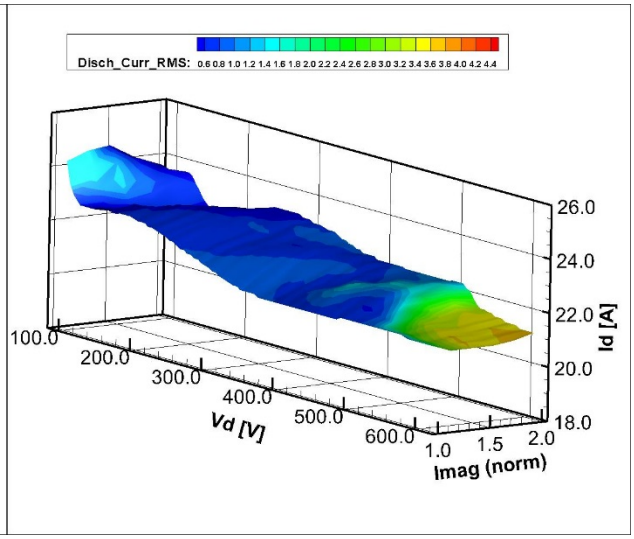

Figure 50. TDU-3 IVB map of discharge current RMS at 20.6mg/s at a CFF of 5% for discharge voltages of 100V to 610V and normalized magnetic field strength of 1 to 2.

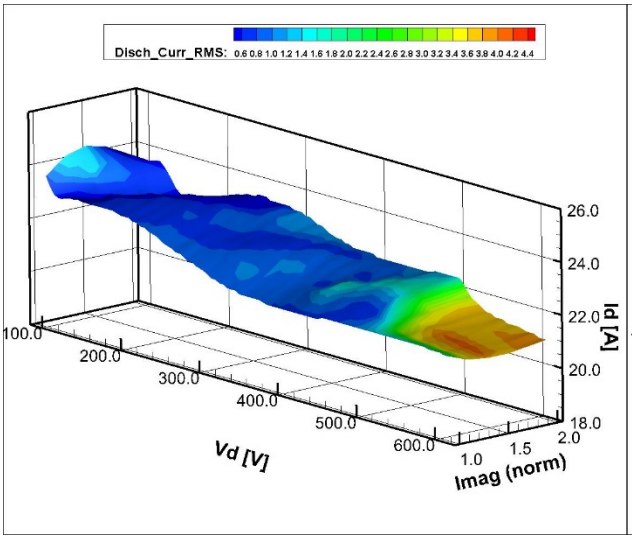

Figure 51. TDU-3 IVB map of discharge current RMS at 20.6mg/s at a CFF of 7% for discharge voltages of 100V to 610V and normalized magnetic field strength of 1 to 2.

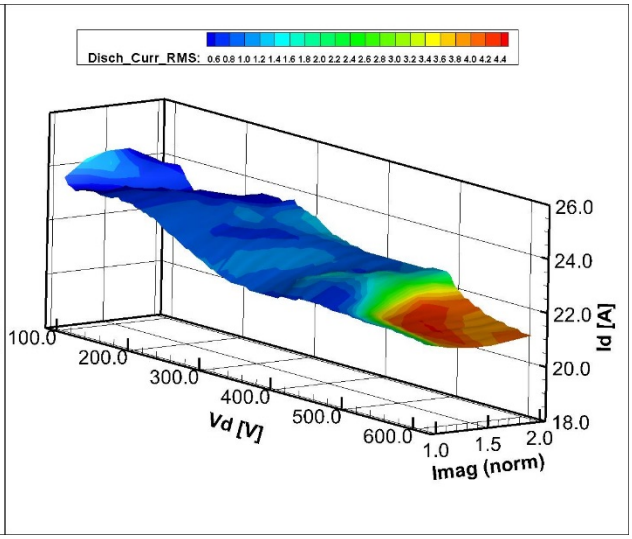

Figure 52. TDU-3 IVB map of discharge current RMS at 20.6mg/s at a CFF of 9% for discharge voltages of 100V to 610V and normalized magnetic field strength of 1 to 2.

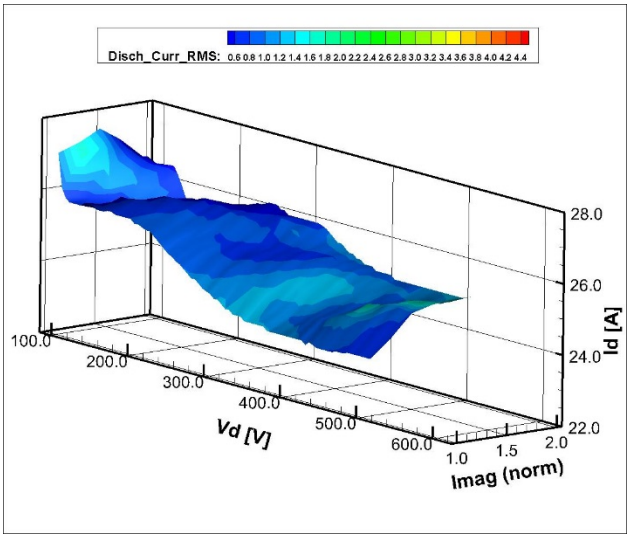

Figure 53. TDU-3 IVB map of discharge current RMS at 22.5mg/s for discharge voltages of 100V to 510V and normalized magnetic field strength of 1 to 2.

VI.Comparison of TDU-1 and TDU-3 Plume Results

Figures 54 to 57 show comparisons of plasma plume properties between the TDU with heritage BN and with BN silica composite discharge channels. Specifically, Fig. 54 shows a comparison of the ion current density profiles, Fig. 55 shows a comparison of the Wien filter spectra, Fig. 56 shows a comparison of the ion energy per charge distribution for 300V operation at a polar angle of -90°, and Fig. 57 shows a comparison of the ion energy per charge distribution for 600V operation at a polar angle of -65°. From these figures, one can conclude that there were negligible difference in the plasma plume characteristics between the TDU with heritage BN grade versus with BN silica composite grade discharge channel material.

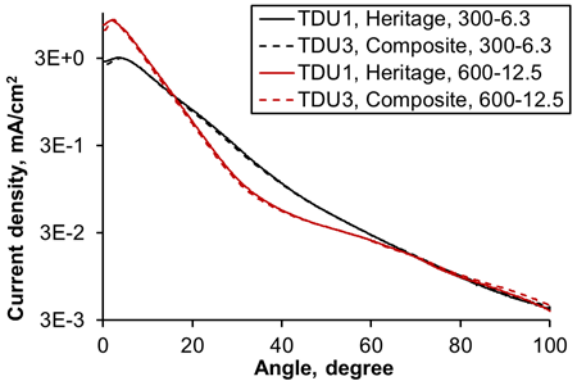

Figure 54. Comparison of ion current density profiles between TDU with heritage versus silica composite boron nitride grades.

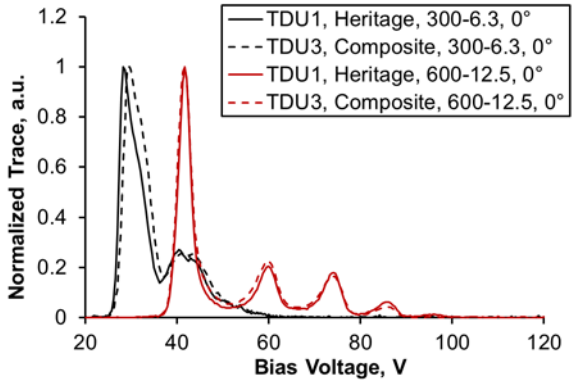

Figure 55. Comparison of Wien filter spectra between TDU with heritage versus silica composite boron nitride grades.

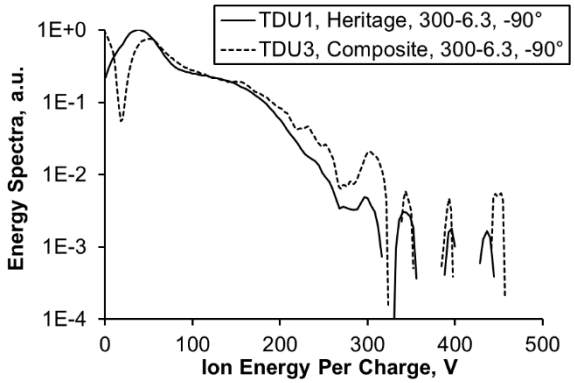

Figure 56. Comparison of ion energy per charge distribution between TDU with heritage versus silica composite boron nitride grades.

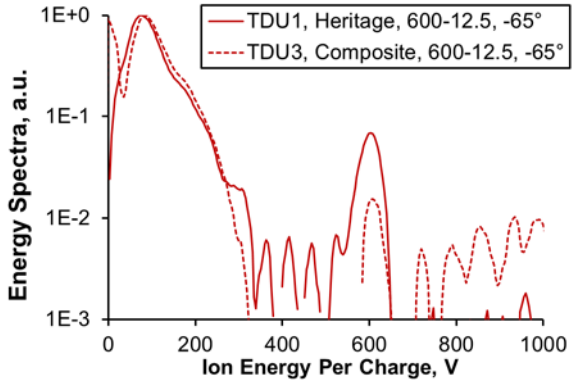

Figure 57. Comparison of ion energy per charge distribution between TDU with heritage versus silica composite boron nitride grades.

VII.Conclusions, Summary, and Future Work

Performance, stability, and plume characterization tests of the HERMeS thruster with a BN silica composite grade discharge channel were performed. The thruster operation was assessed at discharge currents between 5A and 21.8A and discharge voltages between 300V and 600V. Tests were performed for various thruster magnet settings and cathode flow fractions, different harness inductance values, and for reversed electromagnet magnet polarity.

Performance characterization results indicated that the TDU-3 performance with BN silica composite discharge channel material was in family with TDU-1's performance with heritage BN discharge channel material. Tests also revealed that nominal magnetic field setting used for the TDU-1 thruster can be implemented for the TDU-3 thruster and will provide sufficient margin on the magnetic field settings. Cathode flow fraction tests revealed that slightly higher thruster performance can be attained at higher cathode flow fraction. Tests also found that varying the test harness inductance did not appreciably change the thruster's performance.

Stability characterization results indicated that the TDU-3 discharge current Pk2Pk/RMS magnitudes and PSD profiles were similar to TDU-1. Varying the cathode flow fraction between 5% and 9% did not appreciably impact the thruster's stability. IVB maps also indicated profiles that were very similar to the TDU-1 thruster.

Plume maps of the TDU-3 thruster were performed with Faraday, Langmuir, RPA, WFS probes. The plume maps revealed negligible difference in the plasma plume characteristics between the TDU with heritage versus silica composite BN grades.

Conclusions from the performance, stability, and plasma characterization tests of the TDU-3 thruster indicate that switching the discharge channel material from heritage BN grade boron nitride to BN silica composite grade resulted in negligible changes to performance, stability, and plume structure.

Future risk reduction tests will be performed on the TDU-1 and TDU-3 thrusters, these tests will include:

- Long duration tests of TDU-3 thruster (> 3,000hrs) at NASA GRC VF-5;
- Laser induced fluorescence test on TDU-1 at NASA GRC VF-6;[37] and
- Magnetic topology optimization study of the TDU-1 thruster at NASA GRC VF-6.

Acknowledgments

The authors would like to like to thank the Space Technology Mission Directorate through the Solar Electric Propulsion Technology Demonstration Mission Project for funding the joint NASA GRC and JPL development of the Advanced Electric Propulsion System. The authors would also like to thank the many NASA/Aerojet review board members and subject matter experts for providing their expertise and technical guidance to the development of AEPS and its broader Ion Propulsion Subsystem mission application.

References

[1] Smith, B. K., Nazario, M. L., and Cunningham, C. C. "Solar Electric Propulsion Vehicle Demonstration to Support Future Space Exploration Missions," *Space Propulsion 2012*. Bordeaux, France, 2012.

[2] Free, J. "Architecture Status," *NASA Advisory Council Human Exploration and Operations Committee Meeting*. Washington, DC, 2017.

[3] Congress, t. "National Aeronautics and Space Administration Transition Authorization Act of 2017." 2017.

[4] Leiter, H., Kukies, R., Killinger, R., Bonelli, E., Scaranzin, S., Scortecci, F., Neumann, H., and Tartz, M. "RIT-22 Ion Propulsion System: 5,000h Endurance Test Results and Life Prediction." Cincinnati, OH, 2007.

[5] Gerstenmaier, W. "Progress in Defining the Deep Space Gateway and Transport Plan," *NASA Advisory Council Human Exploration and Operations Committee Meeting*, 2017

[6] Jackson, J., et al. "13kW Advanced Electric Propulsion Flight System Development and Qualification," IEPC-2017-223, *35th International Electric Propulsion Conference*. ERPS, Atlanta, GA, 2017.

[7] Hofer, R. R., and Kamhawi, H. "Development Status of a 12.5 kW Hall Thruster for the Asteroid Redirect Robotic Mission," *35th International Electric Propulsion Conference*. ERPS, Atlanta, GA, 2017.

[8] Kamhawi, H., Huang, W., Haag, T. W., Yim, J., Chang, L., Clayman, L., Herman, D. A., Shastry, R., Thomas, R., Griffith, C., Myers, J., Williams, G. J., Mikellides, I., Hofer, R. R., Polk, J. E., and Goebel, D. M. "Overview of the Development of the Solar Electric Propulsion Technology Demonstration Mission 12.5-kW Hall Thruster," *50th AIAA/ASME/SAE/ASEE Joint Propulsion Conference*. Cleveland, OH, 2014.

[9] Kamhawi, H., Haag, T., Huang, W., Herman, D. A., Thomas, R., Shastry, R., Yim, J., Chang, L., Clayman, L., Verhey, T., Griffiths, C., Myers, J., Williams, G., Mikellides, I. G., Hofer, R. R., Polk, J. E., and Jorns, B. A. "Performance Characterization of the Solar Electric Propulsion Technology Demonstration Mission 12.5-kW Hall Thruster," *34th International Electric Propulsion Conference*. Kobe, Japan, 2015.

[10] Hofer, R. R., Kamhawi, H., Herman, D. A., Polk, J. E., Snyder, J. S., Mikellides, I., Huang, W., Myers, J., Yim, J., Williams, G. J., Lopez Ortega, A., Jorns, B., Sekerak, M., Griffiths, C., Shastry, R., Haag, T. W., Verhey, T. R., Gilliam, B., Katz, I., Goebel, D. M., Anderson, J. R., Gilland, J. H., and Clayman, L. "Development Approach and Status of the 12.5 kW HERMeS Hall Thruster for the Solar Electric Propulsion Technology Demonstration Mission," *30th International Electric Propulsion Conference*. Kobe, Hyogo, Japan, 2015.

[11] Myers, J., Kamhawi, H., and Yim, J. "HERMeS Thermal Model," *51st Joint Propulsion Conference*. Orlando, FL, 2015.

[12] Williams, G. J., and Kamhawi, H. "Optical characterization of component wear and near-field plasma of the HERMeS thruster," *62nd JANNAF Propulsion Meeting*. Nashville, TN, 2015.

[13] Kamhawi, H., Haag, T. W., Huang, W., Herman, D. A., Williams, G. J., Peterson, P. Y., Hofer, R. R., and Mikellides, I. "Performance, Stability, and Pressure Effects Characterization Tests of NASA's 12.5-kW Hall Effect Rocket with Magnetic Shielding (HERMeS) Thruster," *52nd AIAA/SAE/ASEE Joint Propulsion Conference*. Salt Lake City, UT, 2016.

[14] Peterson, P. Y., Kamhawi, H., Huang, W., Williams, G., Gilland, J., Yim, J., Hofer, R. R., and Herman, D. "NASA's HERMeS Hall Thruster Electrical Configuration Characterization," *52nd AIAA/ASME/SAE/ASEE Joint Propulsion Conference.* AIAA, Salt Lake City, UT, 2016.

[15] Huang, W., Kamhawi, H., and Haag, T. W. "Facility Effect Characterization Test of NASA's HERMeS Hall Thruster," *52nd AIAA/SAE/ASEE Joint Propulsion Conference*. Salt Lake City, UT, 2016.

[16] Huang, W., Kamhawi, H., and Haag, T. W. "Plasma Oscillation Characterization of NASA's HERMeS Hall Thruster via High Speed Imaging," *52nd AIAA/SAE/ASEE Joint Propulsion Conference*. Salt Lake City, UT, 2016.

[17] Hofer, R. R., and Kamhawi, H. "Development Status of the 12.5 kW HERMeS Hall Thruster Solar Electric Propulsion Technology Demonstration Mission," *52nd AIAA/SAE/ASEE Joint Propulsion Conference.* Salt Lake City, UT, 2016.

[18] Williams, G. J., Gilland, J. H., Peterson, P. Y., Kamhawi, H., Huang, W., Swiatek, M., Joppeck, C., Yim, J., and Haag, T. W. "Wear Testing of the HERMeS Thruster," *52nd AIAA/SAE/ASEE Joint Propulsion Conference*. Salt Lake City, UT, 2016.

[19] Williams, G., Gilland, J. H., Kamhawi, H., Choi, M., Peterson, P. Y., and Herman, D. A. "Wear Trends of the HERMeS Thruster as a Function of Throttle Point," *35th International Electric Propulsion Conference.* ERPS, Atlanta, GA, 2017.

[20] I. Mikellides, I. Katz, R. Hofer, D. Goebel, K. de Grys, and A. Mathers, "Magnetic Shielding of the Acceleration Channel Walls in a Long-Life Hall Thruster," in *Joint Propulsion Conference, AIAA-10-6942*, Nashville, Tennessee 2010.

[21] I. Mikellides, R. R. Hofer, I. Katz, and D. M. Goebel, "Magnetic Shielding of Hall Thrusters at High Discharge Voltages," *Journal of Applied Physics*, vol. 116, 2013.

[22] H. Kamhawi, D. H. Manzella, T. B. Smith, and G. R. Schmidt, "High-Power Hall Propulsion Development at NASA Glenn Research Center," presented at the Space Propulsion 2012, Bordeaux, France, 2012.

[23] R. R. Hofer, H. Kamhawi, I. Mikellides, D. A. Herman, J. E. Polk, W. Huang, *et al.*, "Design Methodology and Scaling of the 12.5 kW HERMeS Hall Thruster for the Solar Electric Propulsion Technology Demonstration Mission," presented at the Presented at the 62nd JANNAF Propulsion Meeting, Nashville, TN, 2015.

[24] Patterson, M. J., and Sovey, J. S. "History of Electric Propulsion at NASA Glenn Research Center: 1956 to Present," *Journal of Aerospace Engineering* Vol. 26, No. 2, 2013, pp. 300-316.

[25] (2016). *NASA GRC Vacuum Facility 5*. Available: https://facilities.grc.nasa.gov/epl/capabilities.html.

[26] J. Yim and J. M. Burt, "Characterization of Vacuum Facility Background Gas Through Simulation and Considerations for Electric Propulsion Ground Testing," in *51st AIAA/SAE/ASEE Joint Propulsion Conference, Propulsion and Energy Forum, AIAA-2015-3825*, Orlando, FL, USA, 2015.

[27] T. W. Haag, "Thrust stand for high-power electric propulsion devices," *Review of Scientific Instruments*, vol. 62, 1991 1991.

[28] T. W. Haag and M. Osborn, "RHETT/EPDM performance characterization," in *International Electric Propulsion Conference, IEPC-97-107*, Cleveland, OH, 1997.

[29] Huang, W., Shastry, R., Soulas, G. C., and Kamhawi, H., "Farfield Plume Measurement and Analysis on the NASA-300M and NASA-300MS", *33rd International Electric Propulsion Conference,* 2013-057, Washington, DC, Oct 6-10, 2013.

[30] Huang, W., Kamhawi, H., and Haag, T., "Effect of Background Pressure on the Performance and Plume of the HiVHAc Hall Thruster", *33rd International Electric Propulsion Conference,* 2013-058, Washington, DC, Oct 6-10, 2013.

[31] Brown, D. L., "Investigation of Flow Discharge Voltage Hall Thruster Characteristics and Evaluation of Loss Mechanisms", Ph.D. Dissertation, Aerospace Engineering, University of Michigan, Ann Arbor, MI, 2009.

[32] R. W. Conversano, R. R. Hofer, M. J. Sekerak, H. Kamhawi, and P. Y. Peterson. Performance comparison of the 12.5 kW HERMeS Hall thruster Technology Demonstration Units. In 52nd AIAA/SAE/ASEE Joint Propulsion Conference, Salt Lake City, UT, July 2016. AIAA-2016-4827.

[33] Pinero, L. "The Impact of Harness Impedance on Hall Thruster Discharge Oscillations," *35th International Electric Propulsion Conference*. ERPS, Atlanta, GA, 2017.

[34] D. L. Brown, R. B. Lobbia, K. D. Hartley, M. Sekerak, D. King, and P. Y. Peterson, "The XR-5 and XR-5A Hall Thrusters, Part 1: Stability and Mode Transitions," in *Joint Army Navy NASA Air Force (JANNAF) conference*, Nashville, TN, 2015.

[35] M. Sekerak, D. L. Brown, R. B. Lobbia, K. D. Hartley, D. King, P. Y. Peterson, *et al.*, "The XR-5 and XR-5A Hall Thrusters, Part 2: Oscillation Behavior," in *Joint Army Navy NASA Air Force (JANNAF) conference*, Nashville, TN, 2015.

[36] Jorns, B. A. and Hofer, R. R., "Plasma oscillations in a 6-kW magnetically shielded Hall thruster, Physics of Plasmas, Vol. 21, No. 5, pp. 053512, 201.

[37] Peterson, P, Kamhawi, H., Huang, W., Yim, J., Haag, T., Mackey J., McVetta, M., Sorelle, L., Tomsik, T., Gillagan, R., and Herman, D. "Reconfiguration of NASA GRC's Vacuum Facility 6 for Testing of Advanced Electric Propulsion System (AEPS) Hardware," *35th International Electric Propulsion Conference.* ERPS, Atlanta, GA, 2017.